An RMVT-Based Finite Rectangular Prism Method for the 3D Analysis of Sandwich FGM Plates with Various Boundary Conditions

Chih-Ping Wu[1,2], Hao-Yuan Li[1]

Abstract: A Reissner's mixed variational theorem (RMVT)-based finite rectangular prism method (FRPM) is developed for the three-dimensional (3D) analysis of sandwich functionally graded material (FGM) plates subjected to mechanical loads, in which the edge conditions of the plates are such that one pair of opposite edges is simply supported and the other pair may be combinations of free, clamped or simply supported edges. The sandwich FGM plate considered consists of two thin and stiff homogeneous material face sheets combined with an embedded thick and soft FGM core, the material properties of which are assumed to obey the power-law distributions of the volume fractions of the constituents. In this formulation, the plate is divided into a number of finite rectangular prisms, in which the trigonometric functions and Lagrange polynomials are used to interpolate the y-direction and $x - \zeta$ plane variations of the primary field variables of each individual prism, respectively. Because an h-refinement process is adopted to yield the convergent solutions in this analysis, the prism-wise either linear or quadratic function distribution through the $x - \zeta$ plane is assumed for the related field variables. A unified formulation of these FRPMs with freely-chosen orders for assorted field variables is presented. It is shown that these quadratic FRPM solutions of simply supported, multilayered composite plates and sandwich FGM ones are in excellent agreement with the exact 3D solutions available in the literature, and those of multilayered composite plates with various boundary conditions closely agree with the solutions obtained using the ANSYS commercial software.

---

[1] Department of Civil Engineering, National Cheng Kung University, Tainan 70101, Taiwan, ROC
[2] Corresponding author. E-mail: cpwu@mail.ncku.edu.tw

1   Introduction

Conventional sandwich plates, composed of two thin and stiff homogeneous face sheets combined with an embedded thick and soft homogeneous core, have been used in various engineering applications, such as in the aerospace and marine engineering industries, in which strong stiff and lightweight components or structures are required. Because the material properties of conventional sandwich plates abruptly change at the interfaces between adjacent layers, huge transverse stresses and discontinuous in-plane stresses will occur at these places, which always result in delamination, cracking and local buckling failures.

In recent decades, a new class of advanced materials, so-called functionally graded materials (FGMs), has been developed and used in the cores of such plates, the material properties of which vary gradually and continuously through the thickness coordinate, eliminating the drawbacks of conventional sandwich plates. The development of theoretical methodologies and numerical modeling approaches for the analysis of these sandwich (or multilayered) FGM structures with various boundary conditions have thus attracted considerable attention, and a number of comprehensive literature surveys of the computational models of multilayered composite plates/shells and FGM ones have been carried out (Noor and Burton, 1990a, b; Noor, Burton and Bert, 1996; Noor, Burton and Peters, 1991; Carrera 2000a, b, 2003a; Carrera and Ciuffreda, 2005a). Among the various computational models proposed in the literature, this article focuses on the exact and approximate three-dimensional (3D) approaches as well as refined and advanced models for the analysis of multilayered FGM (or composite) plates/shells.

Some exact 3D analyses of multilayered FGM (or composite) structures with fully simple supports have been presented. For example, Pan (2003) developed the Stroh formalism for the 3D anisotropic, linearly elastic, and functionally graded rectangular composite laminates, in which the material properties of each individual layer were assumed to vary exponentially through the thickness coordinate. This elegant formalism was applied to the 3D static and free vibration analyses of functionally graded and layered magneto-electro-elastic plates by Pan and Han (2005) and Chen, Chen and Pan (2006), respectively. Kashtalyan (2004), Kashtalyan and Menshykova (2009a) and Woodward and Kashtalyan (2010) presented the 3D elasticity solutions of single-layered FGM plates and sandwich panels with a functionally graded core, the material properties of which were assumed to vary exponentially through the thickness coordinate of the core. A comparative study of sandwich homogeneous and FGM plates showed that the use of a graded core instead of a homogeneous one can eliminate discontinuities of the in-plane normal and shear stresses across the interfaces between the face sheet and the core. This 3D analytical approach was further used by Kashtalyan and Menshykova (2009b) to eval-

uate the effect of a functionally graded interlayer on the 3D elastic deformation of coated plates subjected to transverse loading. The perturbation, multiple time scales and modified Pagano methods were also used for the 3D static, free vibration, buckling, and nonlinear bending analyses of laminated FGM (or composite) elastic, piezoelectric and magneto-electro-elastic plates and shells (Wu and Chiu, 2002; Wu and Chi, 2004, 2005; Wu and Liu, 2007; Wu, Syu and Lo, 2007; Wu and Syu, 2007; Wu and Tsai, 2007; Wu and Huang, 2009; Wu and Lu, 2009; Wu and Jiang, 2011). Finally, a comprehensive literature survey of the 3D analytical approaches of laminated FGM (or composite) plates and shells was undertaken by Wu, Chiu and Wang (2008). However, it is noted that all these above-mentioned 3D analyses were carried out for the plates and shells with fully simply supported conditions, rather than other kinds of boundary conditions.

Some refined and advanced models have also been presented on the basis of the principle of virtual displacements (PVD) and Reissner's mixed variational theorem (RMVT) (Reissner, 1984, 1986) for multilayered composite plates/shells and FGM ones. In the PVD-based theories and numerical models, the displacement components are regarded as the primary variables, and the in-plane stress components can be calculated from these using Hooke's law. While these theories might give accurate predictions of the displacement and in-plane stress components of the deformed plates/shells, they might fail to yield the same accuracy for the transverse shear and normal stresses. A post correction process for the calculation of transverse shear and normal stresses is thus usually needed to improve the accuracy for these stresses, which utilizes the indefinite integrations derived from the stress equilibrium equations. In the RMVT-based theories and numerical models, both the displacement and transverse stress components are regarded as primary variables, and the in-plane stress components can be calculated on the basis of these. The accuracy of the transverse stress components obtained using the RMVT-based approaches is thus much improved in comparison with those obtained using the PVD-based ones. The related developments, ideas, and evaluations based on the RMVT with regard to the modeling of multilayered composite plates/shells were comprehensively described by Carrera (2001) and Carrera, Brischetto, Cinefra and Soave (2010).

Based on the PVD and RMVT, Carrera (2003b) and Carrera and Ciuffreda (2005b) developed a unified formulation to assess theories of multilayered composite elastic structures for various bending problems. In Demasi (2008) this approach was called the "Carrera Unified Formulation" (CUF) and a further generalization, called "Generalized Unified Formulation" (GUF) was presented in the same work. Carrera and Brischetto (2008) and Cinefra, Belouettar, Soave and Carrera (2010) developed a variable kinematic model and introduced it into the CUF for the bending

and free vibration analyses of FGM plates, respectively. Brischetto and Carrera (2010) extensively applied the CUF with RMVT to analyze the mechanical bending problems of FGM plates. Moreover, Demasi (2009a-e) extended GUF to investigate RMVT-based theories, in which a variety of mixed first-order and higher-order shear deformation, zig-zag, layerwise theories were included. Undertaking implementations and comparisons among assorted PVD- and RMVT-based theories of the global and local responses of multilayered orthotropic plates under mechanical loads, Carrera and Petrolo (2010) gave some guidelines and recommendations to construct ones for metallic and composite plates, and Carrera (2000c) concluded that the RMVT-based theories are superior to the PVD-based ones. Again, most of the above-mentioned refined and mixed theories of plates/shells were implemented for the fully simple supports, while little work undertaken with regard to other kinds of boundary conditions.

Some approximate 3D approaches have been developed to investigate the effects of boundary condition on the static behaviors and dynamic responses of laminated FGM (or composite) plates/shells. Chen and *Lüe* (2005), Chen, Lv and Bian (2004), *Lü*, Chen and Shao (2008), and *Lü*, Lim and Chen (2009) developed a state space differential quadrature method for the static and free vibration analyses of laminated composite plates/beams and FGM ones with one pair of simply supported opposite edges and arbitrary boundary conditions at the other pair of opposite edges. Based on a layerwise displacement model combined with the DQ method, Liew, Ng and Zhang (2002) and Zhang, Ng and Liew (2003) studied the 3D bending and free vibration problems of laminated composite plates with clamped and simply supported edges. Liu, Zhang and Zhang (1994) presented the stresses and deformations of rectangular composite plates with various boundary conditions using a mixed high-order shear deformation theory in combination with the state space method, in which a parametric study of the effects of edge conditions, aspect ratios, lamination schemes and loading conditions on the solutions was carried out. On the basis of the 3D elasticity, Sheng and Ye (2002, 2003) developed a state space finite element method (FEM) for the stress analysis of cross-ply laminated composite plates and cylindrical shells, in which the traditional FEMs were used to interpolate the in-plane (or in-surface) variations of state variables, and a state space formulation was introduced to solve the through-thickness stress distributions. This method has also been extensively used to study the free-edge effect in cross-ply laminated composite plates and cylinders subjected to transverse and in-plane loads by Ye and Sheng (2003) and Ye, Sheng and Qin (2004). Ajmi and Benjeddou (2011) developed a discrete-layer finite element method for the electromechanically coupled analysis of piezoelectric adaptive composite structures. In conjunction with the perturbation and DQ methods, Wu and Wu (2000) and

Wu and Tsai (2004) presented the asymptotic DQ solutions for the free vibration analysis of laminated conical shells and for the bending analysis of FGM annular spherical shells, respectively.
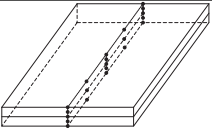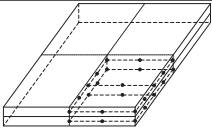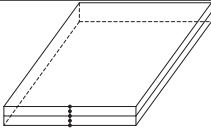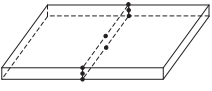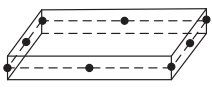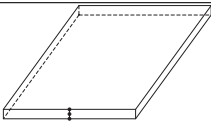
Based on the PVD and RMVT, Carrera and Demasi (2002a, b) presented a unified formulation of finite plate elements for the analysis of multilayered plates, in which both the equivalent single-layered models (ESLMs) preserving the number of variables independent of the number of layers and the layer-wise models (LWMs), in which the variables of each layer constituting the plates remain the same and are independent of one another, were considered.

Based on the PVD, Cheung and Jiang (2001) developed a finite layer method (FLM) for the 3D static analysis of piezoelectric composite laminates, in which the simply-supported laminate was divided into a number of finite layers, and the trigonometric functions and Lagrange polynomials were used to interpolate the in- and out-of-plane variations of the field variables, respectively, for each individual layer. It has been demonstrated that this semi-analytical FLM is more effective in reducing computational effort and core requirements for simply supported laminates. This FLM was also extended to the 3D static, vibration, stability and thermal buckling analyses of piezoelectric composite plates by Akhras and Li (2007, 2008, 2010). Subsequently, based on the RMVT instead of the PVD, Wu and Li (2010a, b) and Wu and Chang (2012) developed a unified formulation of the FLM and the finite cylindrical layer method (FCLM) for the 3D static and free vibration analyses of multilayered FGM (or composite) plates/cylinders, in which the material properties of each individual FGM layer are assumed to obey either an exponent-law exponentially varied with the thickness coordinate or a power-law distribution of the volume fractions of the constituents, and the relative orders used for expansion of the displacement and transverse stress components through the thickness coordinate can be freely chosen.

A close review of the literature, as summarized above, presents the following findings: (a) The RMVT-based theories are superior to the PVD-based ones with regard to predicting the global and local responses of plates/shells. (b) Far fewer published articles deal with the mechanical problems involving FGM plates using RMVT-based theories in comparison with those using the PVD-based ones. (c) All the FLMs are applicable to the 3D problems of multilayered plates/shells with fully simple supports, rather than other kinds of edges such as free and clamped ones. Consequently, the current study was undertaken to develop a unified formulation of the RMVT-based finite rectangular prism method (FRPM) for the 3D analysis of multilayered composite plates and sandwich FGM ones, the edge conditions of which are considered as one pair of simply supported opposite edges and arbitrary combinations of free, clamped or simply supported conditions at the other oppo-

site edges. Because an *h*-refinement process is used for the following illustrative examples, these RMVT-based FRPMs with the relevant orders are taken to be linear or quadratic, which are 4-node linear (L4), 8- and 9-node quadratic (Q8 and Q9) FRPMs. The accuracy and convergence of these FRPMs are investigated by comparing these FRPM solutions with the 3D elasticity solutions available in the literature for the sandwich FGM plates with fully simple supports, and the accurate solutions obtained using an ANSYS commercial software for multilayered composite plates with various boundary conditions. In addition, a parametric study of some effects on the displacement and stress components induced in sandwich FGM plates is carried out, such as the volume fraction exponent, the mid-surface radius-to-thickness ratio and different boundary conditions.

Table 1: Comparisons with regard to the meshes, configuration, interpolation functions, and discretized domains among the present finite rectangular prism, layerwise plate, and finite layer elements.

Elements	Finite rectangular prism elements	Layerwise plate elements	Finite layer elements
Meshes	 (the $2 \times 1 \times 2$ mesh)	 (the 1/4 plate model with a $2 \times 1 \times 2$ mesh)	 (the $1 \times 1 \times 2$ mesh)
Configuration	 (a Q8 prism element)	 (a Q8 shell element)	 (a quadratic layer element)
Interpolation functions	*x*-direction: Lagrange polynomials *y*-direction: Fourier series functions ζ-direction: Lagrange polynomials	x-direction: Lagrange polynomials y-direction: Lagrange polynomials ζ-direction: Power series functions	*x*-direction: Fourier series functions *y*-direction: Fourier series functions ζ-direction: Lagrange polynomials
Discretized domains	$x - \zeta$ plane	$x - y$ plane	ζ-direction

It is noted that the present RMVT-based FRPMs are totally different from the above-mentioned LWM formulation (Carrera and Demasi, 2002a, b) and FLMs (Wu and Li, 2010a, b). In the present formulation, the trigonometric functions and Lagrange polynomials were used to interpolate the *y*-direction and $x - \zeta$ plane variations of the primary field variables of each individual prism element, respectively, while in the LWM formulation the power series functions and Lagrange polynomials were used to interpolate the ζ-direction and $x - y$ plane variations of the primary

field variables of each individual plate element, and in the FLMs, the trigonometric functions and Lagrange polynomials were used to interpolate the $x - y$ plane and the ζ-direction variations of the field variables of each individual layer element. In other words, the present prism element mesh is generated in the $x - \zeta$ plane to form the whole plate, while the plate element mesh in the LWM formulation and FLM meshes are generated in the $x - y$ plane and the ζ-direction, respectively, to form this. Comparisons regarding the meshes, configuration, interpolation functions, and discretized domains among the present FRPMs, LWMs, and FLMs are tabulated in Table 1. Moreover, the comparisons among the solutions obtained using these three formulations will be carried out later in this work.
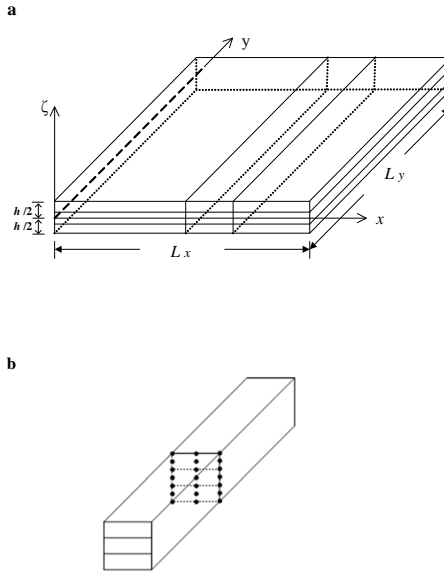
Figure 1: (a) The configuration and coordinates of a sandwich FGM (or homogeneous) plate, and (b) the configuration of a three-layered rectangular prism.

2   The RMVT-Based Finite Prism Method

2.1   The kinematic and kinetic assumptions

We consider a sandwich FGM plate subjected to a sinusoidally (or uniformly) distributed load on the top surface, as shown in Fig. 1*a*, in which the edge conditions of this plate are such that one pair of the opposite edges is simply supported and the other may be combinations of free, clamped or simply supported edges. The

Cartesian global and local coordinate systems (i.e., x, y and ζ coordinates, and $\bar{x}$, $\bar{y}$ and $\bar{\zeta}$ coordinates) are located on the middle plane of the plate and a typical prism, respectively, as shown in Figs. 1a and 1b, in which $x = x_e + \bar{x}$, $y = y_e + \bar{y}$ and $\zeta = \zeta_e + \bar{\zeta}$, and (x_e, y_e, ζ_e) denote the coordinates of the center of the typical prism. L_x and L_y denote the in-plane dimensions of the plate in the x and y directions, respectively. The thicknesses of each individual layer and the plate are h_m $(m = 1, 2, \cdots, N_l)$ and h, respectively, and $h = \sum_{m=1}^{N_l} h_m$, in which N_l is the total number of the layers constituting the plate.

The displacement components of a typical straight and rectangular prism of the mth-layer are given by

$$\left[u_x^{(e)}(x, y, \zeta) \right]^{(m)} = \sum_{i=1}^{n_u} \left[\psi_u^{(e)}(x, \zeta) \right]_i \left[u^{(e)}(y) \right]_i^{(m)}, \tag{1}$$

$$\left[u_y^{(e)}(x, y, \zeta) \right]^{(m)} = \sum_{i=1}^{n_u} \left[\psi_u^{(e)}(x, \zeta) \right]_i \left[v^{(e)}(y) \right]_i^{(m)}, \tag{2}$$

$$\left[u_\zeta^{(e)}(x, y, \zeta) \right]^{(m)} = \sum_{j=1}^{n_w} \left[\psi_w^{(e)}(x, \zeta) \right]_j \left[w^{(e)}(y) \right]_j^{(m)}, \tag{3}$$

where $\left(u^{(e)} \right)_i^{(m)}$, $\left(v^{(e)} \right)_i^{(m)}$, $\left(w^{(e)} \right)_j^{(m)}$ with $(i = 1, 2, \cdots, n_u)$ and $(j = 1, 2, \cdots, n_w)$ are the nodal displacement components of a typical straight and rectangular prism of the mth-layer of the plate; n_i=4, 8 and 9, in which $i = u$ and w, denote the node numbers of the L4, Q8 and Q9 prisms, respectively, the domain of which are $(x_e - a/2) \leq x \leq (x_e + a/2)$, $0 \leq y \leq L_y$ and $(\zeta_e - b/2) \leq \zeta \leq (\zeta_e + b/2)$, in which a and b are the dimensions of the rectangular section of the prism, and their node numberings are shown in Fig. 2; while $\left(\psi_u^{(e)} \right)_i^{(m)}$ $(i = 1, \cdots, n_u)$ and $\left(\psi_w^{(e)} \right)_j^{(m)}$ $(j = 1, 2, \cdots, n_w)$ are the corresponding shape functions, and these are given in the Appendix.

The transverse shear and normal stress components are regarded as the primary variables in the RMVT-based FRPM, and for a typical straight and rectangular prism of the mth-layer these are assumed as follows:

$$\left[\tau_{x\zeta}^{(e)}(x, y, \zeta) \right]^{(m)} = \sum_{i=1}^{n_\tau} \left[\psi_\tau^{(e)}(x, \zeta) \right]_i \left[\tau_{13}^{(e)}(y) \right]_i^{(m)}, \tag{4}$$

$$\left[\tau_{y\zeta}^{(e)}(x, y, \zeta) \right]^{(m)} = \sum_{i=1}^{n_\tau} \left[\psi_\tau^{(e)}(x, \zeta) \right]_i \left[\tau_{23}^{(e)}(y) \right]_i^{(m)}, \tag{5}$$

$$\left[\sigma_\zeta^{(e)}(x, y, \zeta)\right]^{(m)} = \sum_{j=1}^{n_\sigma} \left[\psi_\sigma^{(e)}(x, \zeta)\right]_j \left[\sigma_3^{(e)}(y)\right]_j^{(m)}, \qquad (6)$$

where $\left(\tau_{13}^{(e)}\right)_i^{(m)}$, $\left(\tau_{23}^{(e)}\right)_i^{(m)}$, $\left(\sigma_3^{(e)}\right)_j^{(m)}$ with $(i = 1, 2, \cdots, n_\tau)$ and $(j = 1, 2, \cdots, n_\sigma)$ are the nodal transverse stress components of a typical prism of the mth-layer of the plate; while $\left(\psi_\tau^{(e)}\right)_i$ $(i = 1, 2, \cdots, n_\tau)$ and $\left(\psi_\sigma^{(e)}\right)_j$ $(j = 1, 2, \cdots, n_\sigma)$ are the corresponding shape functions, in which n_τ and n_σ denote the node numbers of the L4, Q8 and Q9 prisms, which are 4, 8 and 9, respectively.
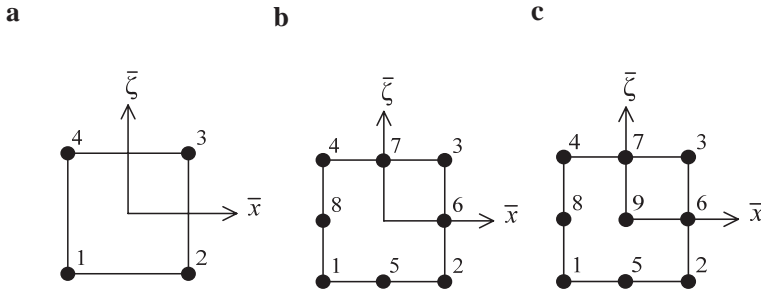
Figure 2: The configuration, coordinates, and node numbering at the nodal plane of the rectangular prisms (a) a L4 prism, (b) a Q8 prism, and (c) a Q9 prism.

Demasi (2009e) indicated that the relative orders used for the expansions of the in-plane and out-of-plane displacements, as well as the transverse shear and normal stresses, are the crucial assumptions for the RMVT-based plate/shell theories, because these assumptions can be the source of numerical instabilities. Implementing a variety of mixed plate theories, Demasi (2009e) concluded that there is no numerical instability if the order of out-of-plane displacement is the same as that of transverse normal stress; otherwise, numerical instability will occur. These conclusions were reexamined and confirmed by Wu and Li (2010a) and Wu and Chang (2012) using the RMVT-based FLMs and FCLMs, respectively. In this work, the orders of various displacements and transverse stresses are thus taken to be identical to one another, in which $n_u = n_w = n_\tau = n_\sigma$, and these values are selected as 4 8 and 9 for L4, Q8 and Q9 FRPMs, respectively.

The linear constitutive equations of the mth-layer, which are valid for the orthotropic

materials, are given by

$$
\left\{
\begin{array}{c}
\sigma_x^{(m)} \\
\sigma_y^{(m)} \\
\sigma_\zeta^{(m)} \\
\tau_{y\zeta}^{(m)} \\
\tau_{x\zeta}^{(m)} \\
\tau_{xy}^{(m)}
\end{array}
\right\}
=
\left[
\begin{array}{cccccc}
c_{11}^{(m)} & c_{12}^{(m)} & c_{13}^{(m)} & 0 & 0 & 0 \\
c_{12}^{(m)} & c_{22}^{(m)} & c_{23}^{(m)} & 0 & 0 & 0 \\
c_{13}^{(m)} & c_{23}^{(m)} & c_{33}^{(m)} & 0 & 0 & 0 \\
0 & 0 & 0 & c_{44}^{(m)} & 0 & 0 \\
0 & 0 & 0 & 0 & c_{55}^{(m)} & 0 \\
0 & 0 & 0 & 0 & 0 & c_{66}^{(m)}
\end{array}
\right]
\left\{
\begin{array}{c}
\varepsilon_x^{(m)} \\
\varepsilon_y^{(m)} \\
\varepsilon_\zeta^{(m)} \\
\gamma_{y\zeta}^{(m)} \\
\gamma_{x\zeta}^{(m)} \\
\gamma_{xy}^{(m)}
\end{array}
\right\},
\tag{7}
$$

where $(\sigma_x^{(m)}, \ \sigma_y^{(m)}, \ \cdots, \ \tau_{xy}^{(m)})$ are the stress components; $(\varepsilon_x^{(m)}, \ \varepsilon_y^{(m)}, \ \cdots, \ \gamma_{xy}^{(m)})$ are the strain components; and $c_{ij}^{(m)}$ are the elastic coefficients, which are constants through the thickness coordinate in the homogeneous elastic layers, and variable through the thickness coordinate in the FG elastic layers (i.e., $c_{ij}^{(m)}(\zeta)$).

The strain-displacement relations for a typical prism of the mth-layer, based on the assumed displacement components in Eqs. (1)–(3), are given by

$$
\begin{aligned}
\left[\varepsilon_x^{(e)}(x, y, \zeta) \right]^{(m)} &= \left(u_x^{(e)},_x \right)^{(m)} \\
&= \sum_{i=1}^{n_u} \left(D_x \psi_u^{(e)} \right)_i \left(u_i^{(e)} \right)^{(m)},
\end{aligned}
\tag{8}
$$

$$
\begin{aligned}
\left[\varepsilon_y^{(e)}(x, y, \zeta) \right]^{(m)} &= \left(u_y^{(e)},_y \right)^{(m)} \\
&= \sum_{i=1}^{n_u} \left(\psi_u^{(e)} \right)_i \left(v_i^{(e)},_y \right)^{(m)},
\end{aligned}
\tag{9}
$$

$$
\begin{aligned}
\left[\varepsilon_\zeta^{(e)}(x, y, \zeta) \right]^{(m)} &= \left(u_\zeta^{(e)},_\zeta \right)^{(m)} \\
&= \sum_{j=1}^{n_w} \left(D_\zeta \psi_w^{(e)} \right)_j \left(w_j^{(e)} \right)^{(m)},
\end{aligned}
\tag{10}
$$

$$
\begin{aligned}
\left[\gamma_{x\zeta}^{(e)}(x, y, \zeta) \right]^{(m)} &= \left(u_x^{(e)},_\zeta \right)^{(m)} + \left(u_\zeta^{(e)},_x \right)^{(m)} \\
&= \sum_{i=1}^{n_u} \left(D_\zeta \psi_u^{(e)} \right)_i \left(u_i^{(e)} \right)^{(m)} + \sum_{j=1}^{n_w} \left(D_x \psi_w^{(e)} \right)_j \left(w_j^{(e)} \right)^{(m)},
\end{aligned}
\tag{11}
$$

$$
\begin{aligned}
\left[\gamma_{y\zeta}^{(e)}(x, y, \zeta) \right]^{(m)} &= \left(u_y^{(e)},_\zeta \right)^{(m)} + \left(u_\zeta^{(e)},_y \right)^{(m)} \\
&= \sum_{i=1}^{n_u} \left(D_\zeta \psi_u^{(e)} \right)_i \left(v_i^{(e)} \right)^{(m)} + \sum_{j=1}^{n_w} \left(\psi_w^{(e)} \right)_j \left(w_j^{(e)},_y \right)^{(m)},
\end{aligned}
\tag{12}
$$

$$\left[\gamma_{xy}^{(e)}(x, y, \zeta)\right]^{(m)} = \left(u_x^{(e)}{}_{,y}\right)^{(m)} + \left(u_y^{(e)}{}_{,x}\right)^{(m)}$$
$$= \sum_{i=1}^{n_u} \left(\psi_u^{(e)}\right)_i \left(u_i^{(e)}{}_{,y}\right)^{(m)} + \sum_{i=1}^{n_u} \left(D_x \psi_u^{(e)}\right)_i \left(v_i^{(e)}\right)^{(m)}, \tag{13}$$

where the commas denote partial differentiation with respect to the suffix variables; and $D_x \psi_j^{(e)} = \frac{d\psi_j^{(e)}}{dx}$, $D_\zeta \psi_j^{(e)} = \frac{d\psi_j^{(e)}}{d\zeta}$, in which $j = u$, w, τ and σ.

2.2   The Reissner mixed variational theorem

The Reissner mixed variational theorem is used to derive the equilibrium equations of the plate, and its corresponding energy functional is written in the form of

$$\Pi_R = \int_{-h/2}^{h/2} \iint_\Omega \left[\sigma_x \varepsilon_x + \sigma_y \varepsilon_y + \sigma_\zeta \varepsilon_\zeta + \tau_{x\zeta}\gamma_{x\zeta} + \tau_{y\zeta}\gamma_{y\zeta} + \tau_{xy}\gamma_{xy} - B(\sigma_{ij})\right] dx\,dy\,d\zeta$$
$$- \iint_{\Omega^+} \left[\bar{q}_k^+(x, y)\, u_k^+(x, y, h/2)\right] dx\,dy - \iint_{\Omega^-} \left[\bar{q}_k^-(x, y)\, u_k^-(x, y, -h/2)\right] dx\,dy$$
$$- \int_{-h/2}^{h/2} \int_{\Gamma_\sigma} (\bar{t}_k u_k)\, d\Gamma\,d\zeta - \int_{-h/2}^{h/2} \int_{\Gamma_u} \left[(u_k - \bar{u}_k) t_k\right] d\Gamma\,d\zeta, \tag{14}$$

where Ω denotes the plate domain on the $x - y$ plane, and Ω^+ and Ω^- denote the top and bottom surfaces of the plate (i.e., $\zeta = h/2$ and $\zeta = -h/2$), respectively, in which the transverse loads $\bar{q}_k^+$ and $\bar{q}_k^-$ ($k = x$, y and ζ) are applied, respectively; Γ_σ and Γ_u denote the portions of the edge boundary, where the surface traction and displacement components (i.e., $\bar{t}_k$, $\bar{u}_k$ ($k = x$, y and ζ)) are prescribed, respectively; and $B(\sigma_{ij})$ is the complementary energy density function.

In the present formulation, we take the displacement and the transverse stress components to be the primary variables subject to variation. Using the kinematic and kinetic assumptions, given in Eqs. (1)–(3) and (4)–(6), the first-order variation of the Reissner energy functional can be expressed as follows:

$$\delta\Pi_R = \sum_{m=1}^{N_l} \sum_{e=1}^{N_e} \left\{ \int_0^{L_y} \int_{\bar{x}-a/2}^{\bar{x}+a/2} \int_{\bar{\zeta}-b/2}^{\bar{\zeta}+b/2} \left\{ \left(\delta\boldsymbol{\varepsilon}_p^{(e)}\right)^T \boldsymbol{\sigma}_p^{(e)} + \left(\delta\boldsymbol{\varepsilon}_s^{(e)}\right)^T \boldsymbol{\sigma}_s^{(e)} + \delta\varepsilon_\zeta^{(e)} \sigma_\zeta^{(e)} + \left(\delta\boldsymbol{\sigma}_s^{(e)}\right)^T \left(\boldsymbol{\varepsilon}_s^{(e)} - \mathbf{S}^{(m)}\boldsymbol{\sigma}_s^{(e)}\right) \right.\right.$$
$$\left.+ \delta\sigma_\zeta^{(e)} \left[\varepsilon_\zeta^{(e)} - \left(c_{33}^{(m)}\right)^{-1}\sigma_\zeta^{(e)} - \left(\mathbf{Q}_\zeta^{(m)}\right)^T \boldsymbol{\varepsilon}_p^{(e)}\right] \right\}^{(m)} d\bar{\zeta}\,d\bar{x}\,dy$$
$$- \sum_{e=1}^{N_e} \int_0^{L_y} \int_{\bar{x}-a/2}^{\bar{x}=a/2} \left\{ \bar{q}_k^+(x, y) \left(\psi_k^{(e)}(\bar{x}, \bar{\zeta} = b/2)\right)_j^{(m=N_l)} \left[u_k^{(e)}(\bar{\zeta} = b/2)\right]_j^{(m=N_l)} \right\} d\bar{x}\,dy$$
$$- \sum_{e=1}^{N_e} \int_0^{L_y} \int_{\bar{x}=-a/2}^{\bar{x}=a/2} \left\{ \bar{q}_k^-(x, y) \left(\psi_k^{(e)}(\bar{x}, \bar{\zeta} = -b/2)\right)_j^{(m=1)} \left[u_k^{(e)}(\bar{\zeta} = -b/2)\right]_j^{(m=1)} \right\} d\bar{x}\,dy$$
$$= 0 \tag{15}$$

where N_e denotes the number of prisms in each individual layer; the superscript of T denotes the transposition of the matrices or vectors; and

$$\boldsymbol{\varepsilon}_p^{(e)} = \left[\begin{array}{ccc} \varepsilon_x^{(e)} & \varepsilon_y^{(e)} & \gamma_{xy}^{(e)} \end{array}\right]^T = \mathbf{B}_1^{(e)} \mathbf{u}^{(e)}, \quad \boldsymbol{\varepsilon}_s^{(e)} = \left[\begin{array}{cc} \gamma_{x\zeta}^{(e)} & \gamma_{y\zeta}^{(e)} \end{array}\right]^T = \mathbf{B}_3^{(e)} \mathbf{u}^{(e)} + \mathbf{B}_4^{(e)} \mathbf{w}^{(e)},$$

$$\boldsymbol{\varepsilon}_{\zeta}^{(e)} = \mathbf{B}_6^{(e)} \mathbf{w}^{(e)}, \quad \boldsymbol{\sigma}_p^{(e)} = \left[\begin{array}{ccc} \sigma_x^{(e)} & \sigma_y^{(e)} & \tau_{xy}^{(e)} \end{array} \right]^T = \mathbf{Q}_p^{(m)} \mathbf{B}_1^{(e)} \mathbf{u}^{(e)} + \mathbf{Q}_\zeta^{(m)} \mathbf{B}_2^{(e)} \boldsymbol{\sigma}^{(e)},$$

$$\boldsymbol{\sigma}_s^{(e)} = \left[\begin{array}{cc} \tau_{x\zeta}^{(e)} & \tau_{y\zeta}^{(e)} \end{array} \right]^T = \mathbf{B}_5^{(e)} \boldsymbol{\tau}^{(e)}, \quad \sigma_\zeta^{(e)} = \mathbf{B}_2^{(e)} \boldsymbol{\sigma}^{(e)},$$

$$\mathbf{u}^{(e)} = \left[\begin{array}{c} u_i^{(e)} \\ v_i^{(e)} \end{array} \right]_{i=1,2,\cdots,n_u}, \quad \mathbf{w}^{(e)} = \left[w_i^{(e)} \right]_{i=1,2,\cdots,n_w},$$

$$\boldsymbol{\tau}^{(e)} = \left[\begin{array}{c} \left(\tau_{13}^{(e)} \right)_i \\ \left(\tau_{23}^{(e)} \right)_i \end{array} \right]_{i=1,2,\cdots,n_\tau}, \quad \boldsymbol{\sigma}^{(e)} = \left[\left(\sigma_3^{(e)} \right)_i \right]_{i=1,2,\cdots,n_\sigma},$$

$$\mathbf{S}^{(m)} = \left[\begin{array}{cc} \left(1/c_{55}^{(m)} \right) & 0 \\ 0 & \left(1/c_{44}^{(m)} \right) \end{array} \right], \quad \mathbf{Q}_p^{(m)} = \left[\begin{array}{ccc} Q_{11}^{(m)} & Q_{12}^{(m)} & 0 \\ Q_{12}^{(m)} & Q_{22}^{(m)} & 0 \\ 0 & 0 & Q_{66}^{(m)} \end{array} \right],$$

$$\mathbf{Q}_\zeta^{(m)} = \left[\begin{array}{c} Q_{13}^{(m)} \\ Q_{23}^{(m)} \\ 0 \end{array} \right],$$

$$\mathbf{B}_1^{(e)} = \left[\begin{array}{cc} \left(D_x \psi_u^{(e)} \right)_i & 0 \\ 0 & \left(\psi_u^{(e)} \right)_i \partial_y \\ \left(\psi_u^{(e)} \right)_i \partial_y & \left(D_x \psi_u^{(e)} \right)_i \end{array} \right]_{i=1,2,\cdots,n_u}, \quad \mathbf{B}_2^{(e)} = \left[\left(\psi_\sigma^{(e)} \right)_i \right]_{i=1,2,\cdots,n_\sigma},$$

$$\mathbf{B}_3^{(e)} = \left[\begin{array}{cc} \left(D_\zeta \psi_u^{(e)} \right)_i & 0 \\ 0 & \left(D_\zeta \psi_u^{(e)} \right)_i \end{array} \right]_{i=1,2,\cdots,n_u}, \quad \mathbf{B}_4^{(e)} = \left[\begin{array}{c} \left(D_x \psi_w^{(e)} \right)_i \\ \left(\psi_w^{(e)} \right)_i \partial_y \end{array} \right]_{i=1,2,\cdots,n_w},$$

$$\mathbf{B}_5^{(e)} = \left[\begin{array}{cc} \left(\psi_\tau^{(e)} \right)_i & 0 \\ 0 & \left(\psi_\tau^{(e)} \right)_i \end{array} \right]_{i=1,2,\cdots,n_\tau}, \quad \mathbf{B}_6^{(e)} = \left[\left(D_\zeta \psi_w^{(e)} \right)_i \right]_{i=1,2,\cdots,n_w},$$

$$Q_{ij}^{(m)} = c_{ij}^{(m)} - \left(c_{i3}^{(m)} c_{j3}^{(m)} / c_{33}^{(m)} \right) \quad (i,j = 1 \text{ and } 2)$$

$$Q_{k3}^{(m)} = c_{k3}^{(m)} / c_{33}^{(m)} \quad (k=1 \text{ and } 2), \quad Q_{66}^{(m)} = c_{66}^{(m)}.$$

2.3 Euler–Lagrange equations

The static behavior of a sandwich FGM plate with the boundary edges and under mechanical loads, such that one pair of the opposite edges at $y{=}0$ and $y = L_y$ is simply supported, and the other two edges at $x{=}0$ and $x = L_x$ are combinations of

free, clamped and simply supported edges, is studied in the following illustrative examples. The applied loading conditions on the lateral surfaces of the plate are prescribed as

$$\left[\tau_{x\zeta}^{(N_l)}(x,y,h/2) \ \tau_{y\zeta}^{(N_l)}(x,y,h/2) \ \sigma_{\zeta}^{(N_l)}(x,y,h/2)\right] = \left[0 \ 0 \ \bar{q}_{\zeta}^{+}(x,y)\right] \ on \ \zeta = h/2$$

(16a)

$$\left[\tau_{x\zeta}^{(1)}(x,y,-h/2) \ \tau_{y\zeta}^{(1)}(x,y,-h/2) \ \sigma_{\zeta}^{(1)}(x,y,-h/2)\right] = [0 \ 0 \ 0] \ on \ \zeta = -h/2$$

(16b)

where $\bar{q}_{\zeta}^{+}$ is expressed as the single Fourier series and given as $\bar{q}_{\zeta}^{+} = \sum\limits_{\hat{n}=1}^{\infty} q_{\hat{n}} \sin(\tilde{n}y)$ in which $\tilde{n} = \hat{n}\pi/L_y$ and $\hat{n}$ is a positive integer.

As above-mentioned, the boundary edges at $y=0$ and $y=L_y$, are simply supported edges, and the corresponding boundary conditions are

$$u_x^{(e)} = u_{\zeta}^{(e)} = \sigma_y^{(e)} = 0. \tag{17}$$

The boundary edges at the other two edges, $x = 0$ and $x = L_x$, are combination of free, clamped or simply supported edges, and the corresponding boundary conditions of these are given as follows:

For free (F) supports,

$$\sigma_x^{(e)} = \tau_{xy}^{(e)} = \tau_{x\zeta}^{(e)} = 0. \tag{18a}$$

For clamped (C) supports,

$$u_x^{(e)} = u_y^{(e)} = u_{\zeta}^{(e)} = 0. \tag{18b}$$

For simple (S) supports,

$$u_y^{(e)} = u_{\zeta}^{(e)} = \sigma_x^{(e)} = 0. \tag{18c}$$

By means of the separation of variables, the primary field variables of each individual layer in Eqs. (1)–(6) are expanded as the single Fourier series so that the boundary conditions of the simply supported edges at $y=0$ and $y = L_y$ are exactly satisfied, and they are rewritten as

$$\left(u_x^{(e)}\right)^{(m)} = \sum_{\hat{n}=1}^{\infty} \sum_{i=1}^{n_u} \left(\psi_u^{(e)}\right)_i \left(u_{\hat{n}}^{(e)}\right)_i^{(m)} \sin \tilde{n} y, \tag{19}$$

$$\left(u_y^{(e)}\right)^{(m)} = \sum_{\hat{n}=1}^{\infty} \sum_{i=1}^{n_u} \left(\psi_u^{(e)}\right)_i \left(v_{\hat{n}}^{(e)}\right)_i^{(m)} \cos\tilde{n}y\,, \tag{20}$$

$$\left(u_\zeta^{(e)}\right)^{(m)} = \sum_{\hat{n}=1}^{\infty} \sum_{j=1}^{n_w} \left(\psi_w^{(e)}\right)_j \left(w_{\hat{n}}^{(e)}\right)_j^{(m)} \sin\tilde{n}y\,, \tag{21}$$

$$\left(\tau_{x\zeta}^{(e)}\right)^{(m)} = \sum_{\hat{n}=1}^{\infty} \sum_{k=1}^{n_\tau} \left(\psi_\tau^{(e)}\right)_k \left(\tau_{13\hat{n}}^{(e)}\right)_k^{(m)} \sin\tilde{n}y\,, \tag{22}$$

$$\left(\tau_{y\zeta}^{(e)}\right)^{(m)} = \sum_{\hat{n}=1}^{\infty} \sum_{k=1}^{n_\tau} \left(\psi_\tau^{(e)}\right)_k \left(\tau_{23\hat{n}}^{(e)}\right)_k^{(m)} \cos\tilde{n}y\,, \tag{23}$$

$$\left(\sigma_\zeta^{(e)}\right)^{(m)} = \sum_{\hat{n}=1}^{\infty} \sum_{l=1}^{n_\sigma} \left(\psi_\sigma^{(e)}\right)_l \left(\sigma_{3\hat{n}}^{(e)}\right)_l^{(m)} \sin\tilde{n}y\,, \tag{24}$$

Introducing the kinetic and kinematic models of the FRPMs (Eqs. (19)–(24)) and the boundary coditions on the lateral surfaces (Eqs. (16a) and (16b)) in Eq. (15), then imposing the stationary principle of the Reissner energy functional (i.e., $\delta\Pi_R = 0$), we thus obtain the Euler–Lagrange equations of the plate as follows:

$$\sum_{m=1}^{N_l} \sum_{e=1}^{N_e} \begin{bmatrix} \mathbf{K}_{\mathrm{I\,I}}^{(e)} & \mathbf{0} & \mathbf{K}_{\mathrm{I\,III}}^{(e)} & \mathbf{K}_{\mathrm{I\,IV}}^{(e)} \\ \mathbf{0} & \mathbf{0} & \mathbf{K}_{\mathrm{II\,III}}^{(e)} & \mathbf{K}_{\mathrm{II\,IV}}^{(e)} \\ \mathbf{K}_{\mathrm{III\,I}}^{(e)} & \mathbf{K}_{\mathrm{III\,II}}^{(e)} & \mathbf{K}_{\mathrm{III\,III}}^{(e)} & \mathbf{0} \\ \mathbf{K}_{\mathrm{IV\,I}}^{(e)} & \mathbf{K}_{\mathrm{IV\,II}}^{(e)} & \mathbf{0} & \mathbf{K}_{\mathrm{IV\,IV}}^{(e)} \end{bmatrix}^{(m)} \begin{bmatrix} \tilde{\mathbf{u}}^{(e)} \\ \tilde{\mathbf{w}}^{(e)} \\ \tilde{\boldsymbol{\tau}}^{(e)} \\ \tilde{\boldsymbol{\sigma}}^{(e)} \end{bmatrix}^{(m)} = \delta_{mN_l} \sum_{e=1}^{N_e} \begin{bmatrix} \mathbf{0} \\ \mathbf{Q}^{(e)} \\ \mathbf{0} \\ \mathbf{0} \end{bmatrix}^{(m)}, \tag{25}$$

where $\left(\mathbf{K}_{i\,j}^{(e)}\right)^{(m)} = \left[\left(\mathbf{K}_{j\,i}^{(e)}\right)^{(m)}\right]^T$ $(i, j = \mathbf{I},\ \mathbf{II},\ \mathbf{III},\ \mathbf{IV})$;

$$\left(\mathbf{K}_{\mathrm{I\,I}}^{(e)}\right)^{(m)} = \int_{-b/2}^{b/2} \int_{-a/2}^{a/2} \left(\tilde{\mathbf{B}}_1^{(e)}\right)^T \mathbf{Q}_p^{(m)} \tilde{\mathbf{B}}_1^{(e)}\, d\bar{x}\, d\bar{\zeta},$$

$$\left(\mathbf{K}_{\mathrm{I\,III}}^{(e)}\right)^{(m)} = \int_{-b/2}^{b/2} \int_{-a/2}^{a/2} \left(\mathbf{B}_3^{(e)}\right)^T \mathbf{B}_5^{(e)}\, d\bar{x}\, d\bar{\zeta},$$

$$\left(\mathbf{K}_{\mathrm{I\,IV}}^{(e)}\right)^{(m)} = \int_{-b/2}^{b/2} \int_{-a/2}^{a/2} \left(\tilde{\mathbf{B}}_1^{(e)}\right)^T \mathbf{Q}_\zeta^{(m)} \mathbf{B}_2^{(e)}\, d\bar{x}\, d\bar{\zeta},$$

$$\left(\mathbf{K}_{\mathrm{II\,III}}^{(e)}\right)^{(m)} = \int_{-b/2}^{b/2} \int_{-a/2}^{a/2} \left(\tilde{\mathbf{B}}_4^{(e)}\right)^T \mathbf{B}_5^{(e)}\, d\bar{x}\, d\bar{\zeta},$$

$$\left(\mathbf{K}_{\mathrm{II\,IV}}^{(e)}\right)^{(m)} = \int_{-b/2}^{b/2} \int_{-a/2}^{a/2} \left(\mathbf{B}_6^{(e)}\right)^T \mathbf{B}_2^{(e)}\, d\bar{x}\, d\bar{\zeta},$$

$$\left(\mathbf{K}_{\text{III III}}^{(e)}\right)^{(m)} = -\int_{-b/2}^{b/2}\int_{-a/2}^{a/2} \left(\mathbf{B}_5^{(e)}\right)^T \mathbf{S}^{(m)} \mathbf{B}_5^{(e)} \, d\bar{x} d\bar{\zeta},$$

$$\left(\mathbf{K}_{\text{IV IV}}^{(e)}\right)^{(m)} = -\int_{-b/2}^{b/2}\int_{-a/2}^{a/2} \left(1/c_{33}^{(m)}\right) \left(\mathbf{B}_2^{(e)}\right)^T \mathbf{B}_2^{(e)} \, d\bar{x} d\bar{\zeta},$$

$$\tilde{\mathbf{B}}_1^{(e)} = \begin{bmatrix} \left(D_x \psi_u^{(e)}\right)_i & 0 \\ 0 & -\tilde{n}\left(\psi_u^{(e)}\right)_i \\ \tilde{n}\left(\psi_u^{(e)}\right)_i & \left(D_x \psi_u^{(e)}\right)_i \end{bmatrix}_{i=1,2,\cdots,n_u}, \qquad \tilde{\mathbf{B}}_4^{(e)} = \begin{bmatrix} \left(D_x \psi_w^{(e)}\right)_i \\ \tilde{n}\left(\psi_w^{(e)}\right)_i \end{bmatrix}_{i=1,2,\cdots,n_w},$$

$$\tilde{\mathbf{u}}^{(m)} = \begin{bmatrix} \left(u_{\hat{n}}^{(e)}\right)_i^{(m)} \\ \left(v_{\hat{n}}^{(e)}\right)_i^{(m)} \end{bmatrix}_{i=1,2,\cdots,n_u}, \qquad \tilde{\mathbf{w}}^{(m)} = \begin{bmatrix} \left(w_{\hat{n}}^{(e)}\right)_i^{(m)} \end{bmatrix}_{i=1,2,\cdots,n_w},$$

$$\tilde{\boldsymbol{\tau}}^{(m)} = \begin{bmatrix} \left(\tau_{13\hat{n}}^{(e)}\right)_i^{(m)} \\ \left(\tau_{23\hat{n}}^{(e)}\right)_i^{(m)} \end{bmatrix}_{i=1,2,\cdots,n_\tau}, \qquad \tilde{\boldsymbol{\sigma}}^{(m)} = \begin{bmatrix} \left(\sigma_{3\hat{n}}^{(e)}\right)_i^{(m)} \end{bmatrix}_{i=1,2,\cdots,n_\sigma},$$

$$\left(\mathbf{Q}^{(e)}\right)^{(m=N_l)} = \int_{-a/2}^{a/2} (q_{\hat{n}}) \mathbf{B}_7^{(e)} \, d\bar{x}, \quad \mathbf{B}_7^{(e)} = \left[\left(\psi_w^{(e)}\left(\bar{x},\bar{\zeta}=b/2\right)\right)_i\right]_{i=1,2,\cdots,n_w}; \text{ and}$$

the symbols of δ_{mN_l} $(m=1,2,\cdots,N_l)$ are the Kronecker delta functions, in which $\delta_{mN_l} = 0$ when $m \neq N_l$, and $\delta_{N_l N_l} = 1$.

It is noted that the determinations of the local stiffness sub-matrices derived and given in Eq. (25), involve a double-integration evaluation, in which the integrands are the multiplication of the related shape functions, the derivatives of these shape functions with respect to x and ζ, and thickness-dependent material properties. A numerical integration technique, the Gaussian quadrature commonly used in the FEMs, is used to evaluate these sub-matrices. To achieve this, a background integration mesh is constructed in the element domain, which is further divided into N_b integration domains along the thickness direction and the $(N_g \times N_g)$-term Gaussian quadrature formula is applied to each background integration domain. The implementation of these FRPMs shows that using N_b=20 and N_g=7 may evaluate each integration to five-decimal accuracy, and this is adopted for the later work of this article.

Using Eq. (25) and assembling the local stiffness matrix and forcing vector of each prism constituting the plate by following the standard process of the FEMs, in which the displacement and transverse stress continuity conditions at the interfaces between adjacent prisms are imposed and thus satisfied a priori for the unified formulation of these RMVT-based FRPMs, it is possible to construct the corresponding global stiffness matrix and forcing vector for the plate. The primary variables at

each node of the prism can then be determined. Subsequently, the variables of in-plane stresses at the nodes can be obtained using the determined primary variables, and these are given by

$$\left(\sigma_x^{(e)}, \ \sigma_y^{(e)}\right)^{(m)} = \sum_{\hat{n}=1}^{\infty} \left(\sigma_{1\hat{n}}^{(e)}, \ \sigma_{2\hat{n}}^{(e)}\right)^{(m)} \sin\tilde{n}y, \tag{26}$$

$$\left(\tau_{xy}^{(e)}\right)^{(m)} = \sum_{n=1}^{\infty} \left(\tau_{12\hat{n}}^{(e)}\right)^{(m)} \cos\tilde{n}y, \tag{27}$$

where $\left[\ \left(\sigma_{1\hat{n}}^{(e)}\right)^{(m)} \ \ \left(\sigma_{2\hat{n}}^{(e)}\right)^{(m)} \ \ \left(\tau_{12\hat{n}}^{(e)}\right)^{(m)} \ \right]^T = \mathbf{Q}_p^{(m)} \tilde{\mathbf{B}}_1^{(e)} \tilde{\mathbf{u}}^{(e)} + \mathbf{Q}_\zeta^{(m)} \mathbf{B}_2^{(e)} \tilde{\sigma}^{(e)}.$

Using this unified formulation of RMVT-based FRPMs, the 3D static behaviors of sandwich FGM plates with various boundary conditions and under mechanical loads are analyzed later in this paper, in which the performance of the RMVT-based L4, Q8 and Q9 FRPMs is also examined.

3   Illustrative examples

3.1   Orthotropic laminated plates

A benchmark problem dealing with the static behaviors of orthotropic three-layered plates (i.e., $\left[0^0/90^0/0^0\right]$) with the fully simple supports and under a sinusoidally distributed load ($\bar{q}_\zeta^+ = q_0 \sin(\pi x/L_x) \sin(\pi y/L_y)$) is presented by Pagano (1970) and other researchers (Wu, Chen and Chiu, 2010; Wu and Tsai, 2012; Wu and Jiang, 2011), and it is used to validate the accuracy and convergence of these RMVT-based L4, Q8 and Q9 FRPMs. The set of normalized variables used in Pagano (1970) is adopted in this example and is given as follows:

$$(\bar{\sigma}_x, \ \bar{\sigma}_y, \ \bar{\tau}_{xy}) = \frac{1}{q_0 S^2} (\sigma_x, \ \sigma_y, \ \tau_{xy}), \quad (\bar{\tau}_{x\zeta}, \ \bar{\tau}_{y\zeta}) = \frac{1}{q_0 S} (\tau_{x\zeta}, \ \tau_{y\zeta}), \quad \bar{\sigma}_\zeta = \frac{\sigma_\zeta}{q_0 S},$$

$$\bar{u}_x = \frac{E_T u_x}{q_0 h S^3}, \quad \bar{u}_\zeta = \frac{100 E_T u_\zeta}{q_0 h S^4}, \quad S = \frac{L_x}{h}. \tag{28}$$

The material properties of the orthotropic elastic material used in Pagano (1970) are adopted as the reference material, which are given as

$$E_L = 25 \text{x} 10^6 \, \text{psi} \ (174.6 \, \text{GPa}), \quad E_T = 1.0 \text{x} 10^6 \, \text{psi} \ (6.89 \, \text{GPa}),$$

$$G_{LT} = 0.5 \text{x} 10^6 \, \text{psi} \ (3.5 \, \text{GPa}), \quad G_{TT} = 0.2 \text{x} 10^6 \, \text{psi} \ (1.4 \, \text{GPa}), \tag{29}$$

$$\upsilon_{LT} = \upsilon_{TT} = 0.25,$$

Table 2: Convergence studies for the RMVT-based FRPM solutions of the displacement and stress components at the crucial positions of $[0°/90°/0°]$ laminated plates with fully simple supports and under the sinusoidally distributed load ($L_y/L_x = 3$).

S (L_x/h)	Theories	$10^2\bar{u}_x$ $\left(0,\frac{L_y}{2},\frac{h}{2}\right)$	$\bar{u}_\zeta$ $\left(\frac{L_x}{2},\frac{L_y}{2},0\right)$	$\bar{\sigma}_x$ $\left(\frac{L_x}{2},\frac{L_y}{2},\frac{h}{2}\right)$	$\bar{\tau}_{xy}$ $(0,0,-\frac{h}{2})$	$\bar{\tau}_{x\zeta}$ $\left(0,\frac{L_y}{2},0\right)$	$\bar{\sigma}_\zeta$ $\left(\frac{L_x}{2},\frac{L_y}{2},0\right)$
4	L4 FRPM (6x6)	-1.4216	2.8627	1.0925	0.0274	0.3137	0.1272
	L4 FRPM (12x12)	-1.4262	2.8320	1.1332	0.0279	0.3642	0.1253
	L4 FRPM (18x18)	-1.4254	2.8264	1.1396	0.0280	0.3466	0.1248
	L4 FRPM (24x24)	-1.4250	2.8240	1.1417	0.0280	0.3544	0.1247
	Q8 FRPM (6x6)	-1.4255	2.8314	1.1658	0.0285	0.3648	0.1248
	Q8 FRPM (12x12)	-1.4247	2.8239	1.1506	0.0282	0.3545	0.1246
	Q8 FRPM (18x18)	-1.4249	2.8226	1.1475	0.0281	0.3526	0.1246
	Q9 FRPM (6x6)	-1.4238	2.8315	1.1684	0.0285	0.3644	0.1249
	Q9 FRPM (12x12)	-1.4247	2.8242	1.1509	0.0282	0.3544	0.1246
	Q9 FRPM (18x18)	-1.4253	2.8230	1.1479	0.0281	0.3526	0.1246
	$LD_{11}(N_l = 9)$	-1.3948	2.8005	1.1219	0.0278	0.3496	0.1245
	$LD_{22}(N_l = 9)$	-1.4240	2.8208	1.1443	0.0281	0.3511	0.1245
	$LM_{11}^{11}(N_l = 9)$	-1.4235	2.8200	1.1437	0.0281	0.3634	0.1246
	$LM_{22}^{22}(N_l = 9)$	-1.4242	2.8211	1.1442	0.0281	0.3483	0.1245
	Exact	NA	2.82	1.14	0.0281	0.351	NA
10	L4 FRPM (6x6)	-0.9195	0.9290	0.6958	0.0120	0.4066	0.0512
	L4 FRPM (12x12)	-0.9173	0.9213	0.7184	0.0122	0.4283	0.0503
	L4 FRPM (18x18)	-0.9169	0.9200	0.7226	0.0122	0.4186	0.0502
	L4 FRPM (24x24)	-0.9167	0.9195	0.7241	0.0123	0.4222	0.0501
	Q8 FRPM (6x6)	-0.9165	0.9226	0.7414	0.0124	0.4272	0.0501
	Q8 FRPM (12x12)	-0.9154	0.9191	0.7292	0.0123	0.4219	0.0500
	Q8 FRPM (18x18)	-0.9140	0.9177	0.7258	0.0123	0.4205	0.0500
	Q9 FRPM (6x6)	-0.9168	0.9230	0.7420	0.0124	0.4272	0.0501
	Q9 FRPM (12x12)	-0.9174	0.9204	0.7307	0.0123	0.4219	0.0500
	Q9 FRPM (18x18)	-0.9191	0.9234	0.7292	0.0123	0.4209	0.0500
	$LD_{11}(N_l = 9)$	-0.9125	0.9164	0.7233	0.0122	0.4200	0.0500
	$LD_{22}(N_l = 9)$	-0.9165	0.9189	0.7260	0.0123	0.4201	0.0500
	$LM_{11}^{11}(N_l = 9)$	-0.9159	0.9189	0.7256	0.0123	0.4201	0.0500
	$LM_{22}^{22}(N_l = 9)$	-0.9165	0.9189	0.7260	0.0123	0.4188	0.0500
	Exact	NA	0.919	0.726	0.0123	0.420	NA

where the subscripts of L and T denote the directions parallel and transverse to the fiber directions, respectively.

Table 2 shows the convergence studies for the L4, Q8 and Q9 FRPM solutions of displacement and stress components induced at the crucial positions of the $\left[0^0/90^0/0^0\right]$ laminated plate with fully simple supports, in which $L_y/L_x = 3$, $S = L_x/h$=4 and 10, and the meshes used in $x - \zeta$ plane are (6x6), (12x12), (18x18) and (24x24) for L4 FRPMs, as well as (6x6), (12x12) and (18x18) for Q8 and Q9 FRPMs. It can be seen in Table 2 that the convergent solutions of Q8 and Q9 FRPMs are obtained with the (18x18) mesh and those of L4 FRPM with the (24x24) mesh, and these are in excellent agreement with the exact 3D solutions (Pagano, 1970) and the quadratic PVD- and RMVT-based FLMs (Wu and Li, 2010a) available in the
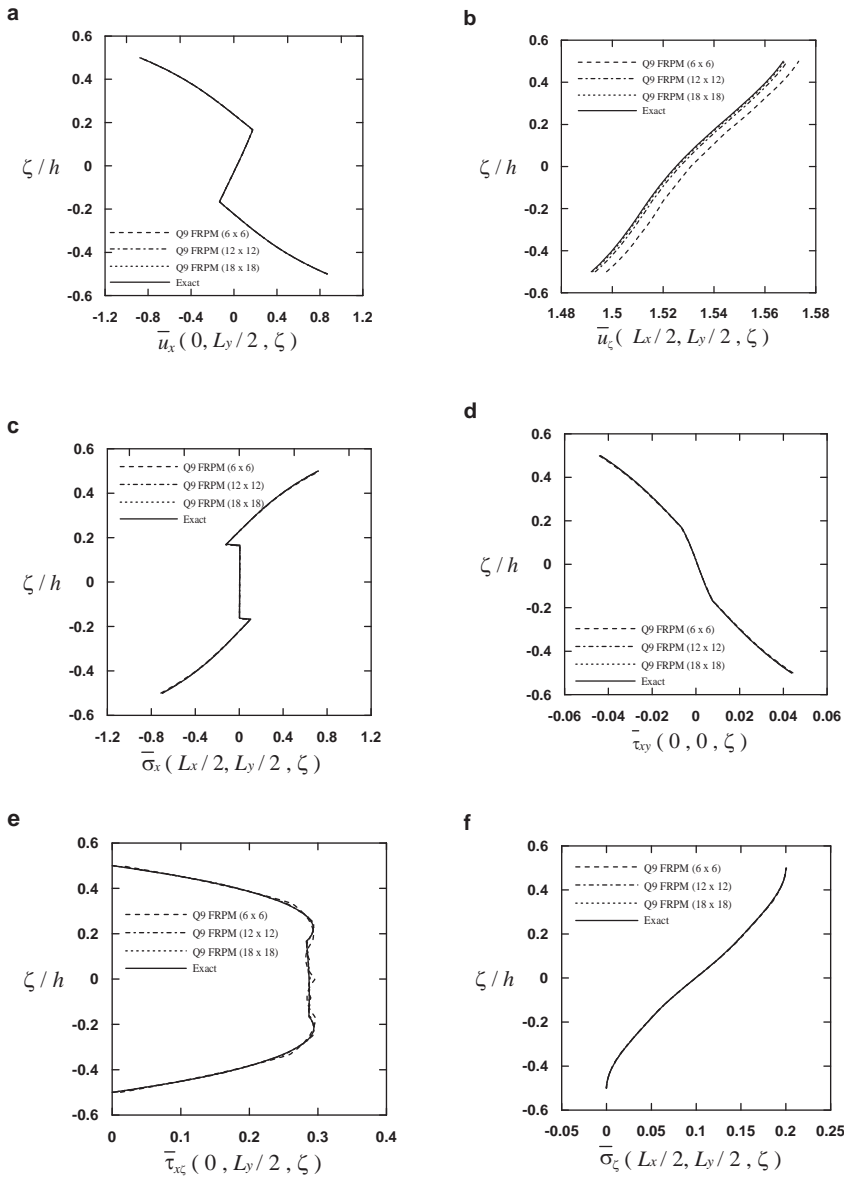
Figure 3: Convergence studies for the Q9 FRPM solutions of the through-thickness distributions of various field variables in a simply-supported, $[0°/90°/0°]$ laminated plate.

literature. Figure 3 shows the convergence studies of the Q9 FRPM for the through-thickness distributions of assorted field variables induced in the simply-supported, $\left[0^0/90^0/0^0\right]$ laminated plates under the sinusoidally distributed load mentioned above, in which $S=5$ and $L_x = L_y$. Again, it is shown that the convergence speed of this Q9 FRPM is rapid, and that the solutions obtained using the (12x12) and (18x18) meshes closely agree with the exact 3D solutions obtained by Wu et al. (2010) using the modified Pagano method (Pagano, 1970).

Table 3: Convergence studies for the RMVT-based FRPM solutions of the displacement and stress components of $[0°/90°/0°]$ laminated plates with various boundary conditions and under a uniformly distributed load $(L_x = L_y, S = 10)$.

Variables	Theories	SS	CC	FF	SC	SF	CF
$\bar{u}_\zeta(L_x/2,L_y/2,0)$	Q9 FRPM (12x12)	1.15554	0.64825	8.73043	0.85500	5.31631	2.44643
	Q9 FRPM (18x18)	1.15580	0.64726	8.73381	0.85452	5.33582	2.44750
	ANSYS (3x30x30)	1.15467	0.64263	8.69467	0.85090	5.28700	2.43430
	ANSYS (6x60x60)	1.15517	0.64663	8.72767	0.85403	5.30200	2.44263
	ANSYS (12x120x120)	1.15540	0.64717	8.72967	0.85447	5.30333	2.44357
	ANSYS (24x120x120)	1.15597	0.64893	8.72100	0.85580	5.29867	2.44390
$\bar{\sigma}_x(L_x/2,L_y/2,h/2)$	Q9 FRPM (12x12)	0.87411	0.40717	0.00461	0.59333	0.38241	-0.21062
	Q9 FRPM (18x18)	0.87304	0.40498	0.00443	0.59317	0.37986	-0.21515
	ANSYS (3x30x30)	0.85209	0.38415	0.00436	0.57330	0.37225	-0.22900
	ANSYS (6x60x60)	0.86441	0.39679	0.00460	0.58638	0.37827	-0.21852
	ANSYS (12x120x120)	0.86859	0.40151	0.00467	0.59096	0.38023	-0.21452
	ANSYS (24x120x120)	0.86988	0.40300	0.00469	0.59239	0.38083	-0.21326
$\bar{\sigma}_\zeta(L_x/2,L_y/2,0)$	Q9 FRPM (12x12)	0.04974	0.04980	0.05002	0.04977	0.04988	0.04991
	Q9 FRPM (18x18)	0.04990	0.04992	0.05001	0.04991	0.04995	0.04996
	ANSYS (3x30x30)	0.05001	0.05000	0.05000	0.05001	0.05001	0.05000
	ANSYS (6x60x60)	0.05001	0.05000	0.05000	0.05001	0.05001	0.05000
	ANSYS (12x120x120)	0.05001	0.05000	0.05000	0.05001	0.05001	0.05000
	ANSYS (24x120x120)	0.05001	0.05000	0.05000	0.05001	0.05001	0.05000

Table 3 shows the Q9 FRPM solutions of displacement and stress components induced at the crucial positions of the $\left[0^0/90^0/0^0\right]$ laminated plates with SS, CC, FF, SC, SF, CF edge conditions and under a uniformly distributed load $(\bar{q}_\zeta^+ = q_0)$, in which $S=10$ and $L_x = L_y$, and the meshes used in $x - \zeta$ plane are (12x12) and (18x18). The uniform load q_0 applied in this work is expanded as a single Fourier series and is given by $q_0 = \sum\limits_{\hat{n}=1, 3, 5}^{N_{\hat{n}}} q_{\hat{n}} \sin{(\hat{n}\pi/L_y)}$ and $q_{\hat{n}} = -4/(\hat{n}\pi)$, in which the total number of terms in the single Fourier series $N_{\hat{n}}$ is adopted as $N_{\hat{n}}=199$. It can be seen in Table 3 that the convergent solutions of Q9 FRPMs are obtained for the plates with various boundary conditions when the (18x18) mesh is used, and these convergent solutions for the plates with other types of supports closely agree with the accurate solutions obtained using the ANSYS software, in which a 20-node brick element with the (24x120x120) mesh in the (ζ, x, y) directions is

used. Moreover, the deflections at the center of the plates with various boundary conditions are FF>SF>CF>SS>SC>CC.

Table 4: Comparisons among the RMVT-based FRPM solutions and layerwise plate element ones of the displacement and stress components at the crucial positions of $[0°/90°/0°]$ laminated square plates with fully simple supports and under the sinusoidally distributed load.

S (L_x/h)	Theories	$\bar{\sigma}_x$ $\left(\frac{L_x}{2},\frac{L_y}{2},\pm\frac{h}{2}\right)$	$\bar{\sigma}_y$ $\left(\frac{L_x}{2},\frac{L_y}{2},\pm\frac{h}{4}\right)$	$\bar{\tau}_{xy}$ $(0,0,\pm\frac{h}{2})$	$\bar{\tau}_{x\zeta}$ $\left(0,\frac{L_y}{2},0\right)$	$\bar{\sigma}_{y\zeta}$ $\left(\frac{L_x}{2},0,0\right)$	$\bar{\sigma}_\zeta$ $\left(\frac{L_x}{2},\frac{L_y}{2},0\right)$	$\bar{u}_\zeta$ $\left(\frac{L_x}{2},\frac{L_y}{2},0\right)$
4	Q9 FRPM (4x4)	0.75084 / -0.71430	0.64896 / -0.65189	-0.04804 / 0.04717	0.23612	0.30556	0.49937	1.95056
	Q9 FRPM (8x8)	0.72881 / -0.69270	0.65900 / -0.66188	-0.04707 / 0.04620	0.22368	0.29527	0.49651	1.94056
	Q9 FRPM (16x16)	0.72270 / -0.68675	0.66170 / -0.66457	-0.04678 / 0.04592	0.22044	0.29249	0.49583	1.93782
	Q9 LM 4 (4x4)	0.7456 / -0.7093	0.6897 / -0.6937	-0.0493 / 0.0484	0.2294	0.3148	0.4964	1.9374
	Exact	0.720 / -0.6840	0.663 / -0.6660	-0.0467 / 0.0458	0.219	0.292	NA	1.937
10	Q9 FRPM (4x4)	0.58433 / -0.58500	0.40178 / -0.40335	-0.02815 / 0.02829	0.31270	0.21100	0.50152	0.74384
	Q9 FRPM (8x8)	0.56563 / -0.56616	0.40097 / -0.40254	-0.02770 / 0.02784	0.30407	0.20047	0.50009	0.73881
	Q9 FRPM (16x16)	0.56105 / -0.56156	0.40121 / -0.40278	-0.02758 / 0.02772	0.30197	0.19725	0.49990	0.73796
	Q9 LM 4 (4x4)	0.5909 / -0.5915	0.4225 / -0.4244	-0.0286 / 0.0287	0.3073	0.1607	0.5018	0.7376
	Exact	0.559 / -0.559	0.401 / -0.403	-0.0275 / 0.0276	0.301	0.196	NA	0.737
20	Q9 FRPM (4x4)	0.56829 / -0.56873	0.31068 / -0.31111	-0.02343 / 0.02348	0.33906	0.17045	0.50135	0.51803
	Q9 FRPM (8x8)	0.54959 / -0.54999	0.30873 / -0.30915	-0.02315 / 0.02320	0.33084	0.16175	0.50012	0.51423
	Q9 FRPM (16x16)	0.54475 / -0.54513	0.30849 / -0.30891	-0.02307 / 0.02311	0.32902	0.15769	0.50003	0.51342
	Q9 LM 4 (4x4)	0.5732 / -0.5741	0.3239 / -0.3247	-0.0239 / 0.0240	0.3592	0.1697	0.5342	0.5133
	Exact	0.543 / -0.5430	0.308 / -0.3090	-0.0230 / 0.0230	0.328	0.156	NA	0.513
100	Q9 FRPM (4x4)	0.56468 / -0.56470	0.27387 / -0.27386	-0.02165 / 0.02166	0.34658	0.15149	0.50127	0.43901
	Q9 FRPM (8x8)	0.54577 / -0.54579	0.27179 / -0.27178	-0.02144 / 0.02145	0.34139	0.14953	0.50007	0.43584
	Q9 FRPM (16x16)	0.54128 / -0.54130	0.27154 / -0.27153	-0.02141 / 0.02141	0.34088	0.14851	0.49999	0.43549
	Q9 LM 4 (4x4)	0.5655 / -0.5655	0.2841 / -0.2841	-0.0224 / 0.0224	0.3665	0.1505	0.5302	0.4348
	Exact	0.539 / -0.539	0.271 / -0.271	-0.0214 / 0.0214	0.339	0.139	NA	0.435

Table 4 shows the comparisons between the solutions obtained using the present RMVT-based FRPMs and the RMVT-based layerwise formulation of plate elements (Carrera and Demasi, 2002a, b), in which the bending of simply-supported, $[0^0/90^0/90^0/0^0]$ laminated square plates under a sinusoidally distributed load ($\bar{q}_\zeta^+ = q_0 \sin(\pi x/L_x)\sin(\pi y/L_y)$) is considered. Again, it is shown that the Q9 LM4 solutions with a (4x4) mesh closely agree the present Q9 FRPM ones although the mesh in LM4 is generated in the $x - y$ plane, while this in the present FRPM is generated in the $x - \zeta$ plane. In addition, the present Q9 FRPM solutions converge

rapidly, and their solutions with a (16x16) mesh are in excellent agreement with the exact 3D solutions (Pagano, 1970).

Table 5: The displacement and stress components at the crucial positions of single-layered FGM plates with fully simple supports and under a sinusoidally distributed load ($L_x = L_y, S = 10, h = 0.1m$).

κ_p	Theories	$\hat{u}_x$ $\left(0, \frac{L_y}{2}, -\frac{h}{4}\right)$	$\hat{u}_\zeta$ $\left(\frac{L_x}{2}, \frac{L_y}{2}, 0\right)$	$\hat{\sigma}_y$ $\left(\frac{L_x}{2}, \frac{L_y}{2}, \frac{h}{3}\right)$	$\hat{\tau}_{xy}$ $\left(0, 0, -\frac{h}{3}\right)$	$\hat{\tau}_{y\zeta}$ $\left(\frac{L_x}{2}, 0, \frac{h}{6}\right)$	$\hat{\sigma}_\zeta$ $\left(\frac{L_x}{2}, \frac{L_y}{2}, 0\right)$
1	Q9 FRPM (6x6)	0.6436	0.5901	1.5153	0.6172	0.2716	0.0398
	Q9 FRPM (12x12)	0.6437	0.5883	1.5085	0.6130	0.2577	0.0397
	Q9 FRPM (18x18)	0.6435	0.5878	1.5069	0.6119	0.2541	0.0397
	$LD_{22}(N_l = 10)$	0.6436	0.5875	1.5060	0.6112	0.2504	0.0398
	$LM_{22}^{22} (N_l = 10)$	0.6436	0.5875	1.5061	0.6112	0.2503	0.0397
	RMVT-based TSDT	0.6414	0.5890	1.4898	0.6111	0.2506	NA
	Generalized SDT	0.6626	0.5889	1.4894	0.6110	0.2622	NA
	VK model ($N_l = 100$)	0.6436	0.5875	1.5062	0.6081	0.2510	NA
2	Q9 FRPM (6x6)	0.9011	0.7603	1.4214	0.5490	0.2692	0.0388
	Q9 FRPM (12x12)	0.9014	0.7578	1.4148	0.5452	0.2560	0.0388
	Q9 FRPM (18x18)	0.9021	0.7576	1.4139	0.5446	0.2526	0.0387
	$LD_{22} (N_l = 10)$	0.9013	0.7570	1.4128	0.5436	0.2492	0.0390
	$LM_{22}^{22} (N_l = 10)$	0.9013	0.7570	1.4130	0.5436	0.2490	0.0387
	RMVT-based TSDT	0.8984	0.7573	1.3960	0.5442	0.2491	NA
	Generalized SDT	0.9281	0.7573	1.3954	0.5441	0.2763	NA
	VK model ($N_l = 100$)	0.9012	0.7570	1.4147	0.5421	0.2496	NA
4	Q9 FRPM (6x6)	1.0542	0.8862	1.2008	0.5728	0.2520	0.0406
	Q9 FRPM (12x12)	1.0544	0.8832	1.1956	0.5687	0.2412	0.0404
	Q9 FRPM (18x18)	1.0538	0.8822	1.1940	0.5675	0.2384	0.0404
	$LD_{22} (N_l = 10)$	1.0541	0.8823	1.1941	0.5671	0.2359	0.0407
	$LM_{22}^{22} (N_l = 10)$	1.0541	0.8823	1.1942	0.5671	0.2358	0.0404
	RMVT-based TSDT	1.0502	0.8815	1.1794	0.5669	0.2360	NA
	Generalized SDT	1.0941	0.8819	1.1783	0.5667	0.2580	NA
	VK model (N_l=100)	1.0541	0.8823	1.1985	0.5666	0.2362	NA
8	Q9 FRPM (6x6)	1.0831	0.9782	0.9673	0.5943	0.2391	0.0418
	Q9 FRPM (12x12)	1.0832	0.9748	0.9634	0.5900	0.2299	0.0416
	Q9 FRPM (18x18)	1.0825	0.9745	0.9632	0.5890	0.2279	0.0416
	$LD_{22}(N_l = 10)$	1.0830	0.9738	0.9622	0.5883	0.2250	0.0414
	$LM_{22}^{22} (N_l = 10)$	1.0830	0.9738	0.9624	0.5883	0.2258	0.0416
	RMVT-based TSDT	1.0763	0.9747	0.9477	0.5858	0.2263	NA
	Generalized SDT	1.1340	0.9750	0.9466	0.5856	0.2121	NA
	VK model ($N_l = 100$)	1.0830	0.9738	0.9687	0.5879	0.2262	NA

3.2   Single-layered FGM plates

The static behaviors of single-layer FGM plates with various boundary conditions and under a sinusoidally distributed load ($\bar{q}_\zeta^+ = q_0 \sin(\pi x/L_x) \sin(\pi y/L_y)$) are investigated. The total thickness of the plate is considered to be 0.1m, and the side-to-thickness ratio S (or L_x/h) to be 10 in Tables 5 and 6. The plates are made of Aluminum (bottom) and Alumina (top), for which the Young's modulus ($E(\zeta)$)

obeys a power-law distribution throughout the thickness coordinate, while the Poisson's ratio ($\upsilon(\zeta)$) remains constant, as given by

$$E(\zeta) = E_m + (E_c - E_m)\left(\frac{2\zeta + h}{2h}\right)^{\kappa_p} \qquad -h/2 \leq \zeta \leq h/2, \qquad (30)$$

$$\upsilon(\zeta) = 0.3 \qquad -h/2 \leq \zeta \leq h/2, \qquad (31)$$

where the subscripts of *m* and *c* denote the metal (Aluminum) and ceramic (Alumina) materials constituting the bottom and top layers, respectively; $E_m = 70$ GPa and $E_c = 380$ Gpa; and κ_p is the volume fraction exponent.

This static problem was studied by Carrera, Brischetto and Robaldo (2008) using a discrete layer theory combined with a variable kinematic (VK) model, and then re-examined by Zenkour (2006) using a generalized shear deformation theory (SDT), by Wu and Li (2010c) using an RMVT-based third-order shear deformation theory (TSDT), and by Wu and Li (2010a) using the PVD- and RMVT-based FLMs. For comparison purposes a set of dimensionless variables is adopted, as used in several earlier works mentioned above, and this is given by

$$\hat{u}_x = \left(\frac{100\,h^3 E_c}{L_x^4 q_0}\right)u_x, \quad \hat{u}_y = \left(\frac{100\,h^3 E_c}{L_x^4 q_0}\right)u_y, \quad \hat{u}_\zeta = \left(\frac{10\,h^3 E_c}{L_x^4 q_0}\right)u_\zeta,$$

$$(\hat{\sigma}_x, \ \hat{\sigma}_y, \ \hat{\tau}_{xy}) = \left(\frac{h}{L_x q_0}\right)(\sigma_x, \ \sigma_y, \ \tau_{xy}), \quad (\hat{\tau}_{x\zeta}, \ \hat{\tau}_{y\zeta}) = \left(\frac{h}{L_x q_0}\right)(\tau_{x\zeta}, \ \tau_{y\zeta}),$$

$$\hat{\sigma}_\zeta = \left(\frac{h}{L_x q_0}\right)\sigma_\zeta. \qquad (32)$$

Table 5 shows the Q9 FRPM solutions of displacement and stress components induced at the crucial positions of the plates with fully simple supports (i.e., SS supports) and under a sinusoidally distributed load, in which (6x6), (12x12) and (18x18) meshes are used, and the values of κ_p are taken to be 1, 2, 4 and 8. It can be seen that the convergent solutions Q9 FRPM are yielded when (18x18) mesh is used, and they are in excellent agreement with the convergent solutions obtained by Carrera, Brischetto and Robaldo (2008) using a discrete layer theory with a VK model, and those obtained by Wu and Li (2010a) using the PVD- and RMVT-based quadratic FLMs.

Table 6 shows the Q8 and Q9 FRPM solutions of displacement and stress components induced at the crucial positions of the plates with various boundary conditions and under a sinusoidally distributed load, in which (12x12) and (18x18) meshes are used, and κ_p=3. Again, it is shown that the deflections at the center of the FGM plates with various boundary conditions are FF>SF>CF>SS>SC>CC. These solutions may provide a reference for assessing the solutions obtained using other

numerical modeling approaches, because there are quite a few exact 3D solutions of FGM plates with various boundary conditions in the open literature, and that most commercial software is not able to handle the mechanical problems involving FGM structures.

Table 6: The RMVT-based Q8 and Q9 FRPM solutions of the displacement and stress components of single-layered FGM plates with various boundary conditions and under a sinusoidally distributed load ($\kappa_p = 3, L_x = L_y, S = 10, h = 0.1m$).

Variables	Present	SS	CC	FF	SC	SF	CF
$\hat{u}_\zeta(L_x/2, L_y/2, 0)$	Q8 FRPM (12x12)	0.8391	0.4612	2.1408	0.6164	1.3993	1.0311
	Q8 FRPM (18x18)	0.8385	0.4610	2.1413	0.6162	1.3988	1.0309
	Q9 FRPM (12x12)	0.8393	0.4613	2.1411	0.6166	1.3997	1.0314
	Q9 FRPM (18x18)	0.8385	0.4610	2.1416	0.6162	1.3989	1.0310
$\hat{\sigma}_x(L_x/2, L_y/2, h/2)$	Q8 FRPM (12x12)	3.9092	2.9406	2.7213	3.2926	3.3966	2.7220
	Q8 FRPM (18x18)	3.8987	2.9261	2.7100	3.3451	3.3681	2.6789
	Q9 FRPM (12x12)	3.9094	2.9411	2.7217	3.2917	3.3973	2.7231
	Q9 FRPM (18x18)	3.9006	2.9266	2.7098	3.3472	3.3678	2.6768
$\hat{\sigma}_\zeta(L_x/2, L_y/2, 0)$	Q8 FRPM (12x12)	0.0396	0.0403	0.0395	0.0400	0.0396	0.0401
	Q8 FRPM (18x18)	0.0395	0.0398	0.0395	0.0397	0.0395	0.0397
	Q9 FRPM (12x12)	0.0396	0.0404	0.0396	0.0401	0.0396	0.0402
	Q9 FRPM (18x18)	0.0396	0.0399	0.0396	0.0398	0.0396	0.0398

3.3 Sandwich FGM plates

The static behaviors of sandwich FGM plates, which consist of two thin homogeneous face-sheets and a thick FGM core, with various boundary conditions and under a sinusoidally distributed load ($\bar{q}_\zeta^+ = q_0 \sin(\pi x/L_x) \sin(\pi y/L_y)$), are examined in this section. The thickness ratio of each layer of the sandwich cylinder is $h_1 : h_2 : h_3$, in which $h_1 = h_3$ and $\sum_{m=1}^{3} h_m = h$, and the effective engineering constants of each layer are as follows:

$$E^{(m)}(\zeta) = E_0 + (E_f - E_0)\, \Gamma^{(m)}(\zeta) \qquad (m = 1, 2 \text{ and } 3) \tag{33a}$$

$$\upsilon^{(m)} = \text{constant} \qquad (m = 1, 2 \text{ and } 3), \tag{33b}$$

where E_0 and E_f denote the Young's modulus of the material at the mid-surface of the core-layer and that of the face-sheets, respectively, for which E_0=70 GPa (Aluminum) and E_f=380 GPa (Alumina) are used in this example; $\upsilon^{(m)}$ (m=1–3) are taken to be 0.3; and $\Gamma^{(m)}$ (m=1–3) are the volume fractions of the constituents of the cylinder, and are given by

$$\Gamma^{(1)} = 1 \qquad\qquad when \qquad (-h/2) \le \zeta \le (-h_2/2), \tag{34a}$$

$$\Gamma^{(2)}(\zeta) = [\,|\zeta|\,/\,(h_2/2)\,]^{\kappa_p} \qquad when \qquad (-h_2/2) \le \zeta \le (h_2/2), \qquad (34b)$$

$$\Gamma^{(3)} = 1 \qquad\qquad when \qquad (h_2/2) \le \zeta \le (h/2). \qquad (34c)$$

It is apparent that when $\kappa_p=0$, $\Gamma^{(2)} = 1$, this FGM sandwich cylinder reduces to a single-layered homogeneous isotropic plate with material properties E_f=380 GPa and υ_f=0.3; while when $\kappa_p = \infty$, $\Gamma^{(2)} = 0$, this sandwich FGM plate reduces to a homogeneous sandwich plate with material properties $E^{(1)} = E^{(3)}$=380 GPa, $E^{(2)}$=70 GPa, and $\upsilon^{(m)}$=0.3 (m=1–3). The through-thickness distributions of Young's modulus with different values of κ_p are shown in Fig. 4, in which κ_p=0, 1, 3 and ∞. In addition, a set of dimensionless variables used in example 3.2 (i.e., Eq. (32) is adopted in the following cases, except that E_c in the dimensionless form of displacement components is replaced by E_f.
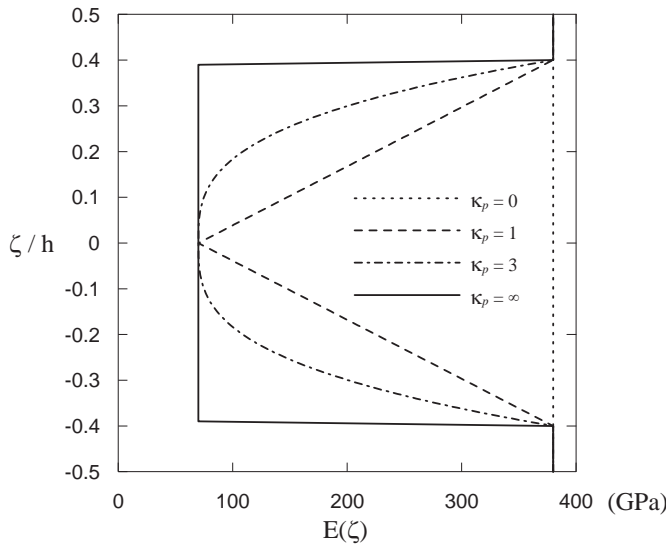

Figure 4: The variations of the through-thickness distributions of the Young's modulus of the sandwich FGM plate with $\kappa_p = 0, 1, 3$ and ∞.

Figure 5 shows the Q9 FRPM solutions for the through-thickness distributions of displacement and stress components induced in the simply supported, sandwich FGM plates with different values of κ_p, in which L_x/h=5, $L_x = L_y$, $h_1 : h_2 : h_3$=0.1h:0.8h:0.1h, and κ_p=0, 3 and ∞. It can be seen in Fig. 5 that the through-thickness distributions of the in-plane displacement/stress and the transverse shear stress components for single-layered homogeneous ($\kappa_p = 0$), sandwich homogeneous ($\kappa_p = \infty$), and sandwich FGM ($\kappa_p \ne 0$ and ∞) plates differ from one another, and that these distributions are global linear and global parabolic functions

for single-layered homogeneous plates, layerwise linear and parabolic functions for sandwich homogeneous plates, and layerwise higher-order polynomial functions for sandwich FGM plates.
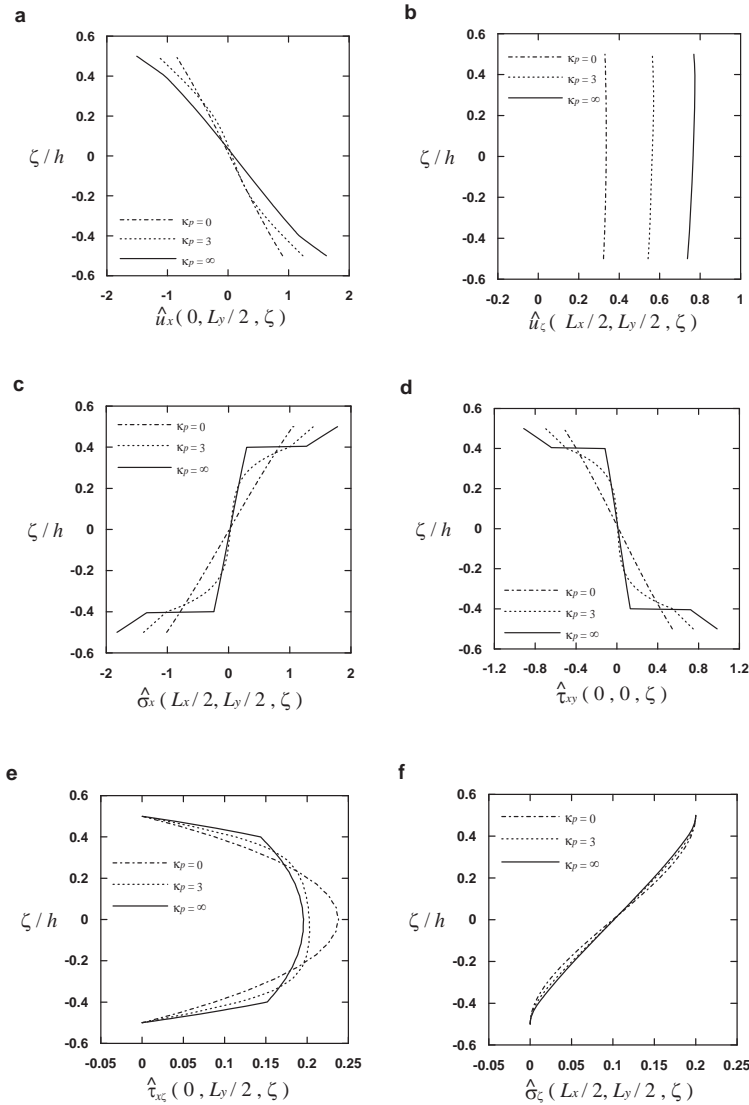

Figure 5: The Q9 FRPM solutions for the through-thickness distributions of various field variables of the simply supported, sandwich FGM plates with different values of κ_p, in which $\kappa_p = 0, 3$ and ∞.

Figure 5 also shows that the in-surface stresses are continuously distributed through the interfaces between the face-sheet and core layers for sandwich FGM cylinders ($\kappa_p \neq \infty$), but change abruptly for the sandwich homogeneous cylinders ($\kappa_p = \infty$). Moreover, the transverse shear stresses induced at the face-sheet/core interfaces for sandwich FGM cylinders are reduced in comparison with those for sandwich homogeneous cylinders, and the introduction of the functionally graded core also decrease both the in- and out-of-surface displacements induced in the cylinders.

Table 7: The displacement and stress components at the centers of sandwich FGM plates with various boundary conditions and under a sinusoidally distributed load ($L_x = L_y$).

κ_p	S (L_x/h)	Variables	Theories	SS	CC	FF	SC	SF	CF
1	5	$\hat{u}_\zeta(L_x/2, L_y/2, 0)$	Q9 FRPM (6x6)	0.4349	0.3115	0.9775	0.3657	0.6728	0.5587
			Q9 FRPM (12x12)	0.4446	0.3159	1.0093	0.3726	0.6903	0.5702
			Q9 FRPM (18x18)	0.4441	0.3154	1.0096	0.3721	0.6897	0.5695
		$\hat{\sigma}_x(L_x/2, L_y/2, 0)$	Q9 FRPM (6x6)	0.0310	0.0295	0.0331	0.0303	0.0318	0.0309
			Q9 FRPM (12x12)	0.0326	0.0317	0.0318	0.0323	0.0321	0.0319
			Q9 FRPM (18x18)	0.0332	0.0323	0.0324	0.0328	0.0327	0.0325
		$\hat{\sigma}_\zeta(L_x/2, L_y/2, 0)$	Q9 FRPM (6x6)	0.0878	0.0883	0.0879	0.0880	0.0879	0.0881
			Q9 FRPM (12x12)	0.0977	0.0980	0.0978	0.0979	0.0978	0.0979
			Q9 FRPM (18x18)	0.0991	0.0992	0.0992	0.0992	0.0991	0.0992
1	10	$\hat{u}_\zeta(L_x/2, L_y/2, 0)$	Q9 FRPM (6x6)	0.3384	0.1981	0.8404	0.2562	0.5560	0.4211
			Q9 FRPM (12x12)	0.3467	0.2019	0.8677	0.2622	0.5714	0.4314
			Q9 FRPM (18x18)	0.3465	0.2018	0.8683	0.2621	0.5713	0.4313
		$\hat{\sigma}_x(L_x/2, L_y/2, 0)$	Q9 FRPM (6x6)	0.0202	0.0176	0.0255	0.0187	0.0224	0.0203
			Q9 FRPM (12x12)	0.0168	0.0163	0.0164	0.0166	0.0166	0.0164
			Q9 FRPM (18x18)	0.0171	0.0166	0.0167	0.0169	0.0169	0.0167
		$\hat{\sigma}_\zeta(L_x/2, L_y/2, 0)$	Q9 FRPM (6x6)	0.0436	0.0436	0.0436	0.0436	0.0436	0.0436
			Q9 FRPM (12x12)	0.0486	0.0486	0.0486	0.0486	0.0486	0.0486
			Q9 FRPM (18x18)	0.0493	0.0493	0.0493	0.0493	0.0493	0.0493
3	5	$\hat{u}_\zeta(L_x/2, L_y/2, 0)$	Q9 FRPM (6x6)	0.5650	0.4260	1.2220	0.4881	0.8542	0.7283
			Q9 FRPM (12x12)	0.5635	0.4224	1.2297	0.4857	0.8543	0.7247
			Q9 FRPM (18x18)	0.5628	0.4216	1.2298	0.4850	0.8534	0.7235
		$\hat{\sigma}_x(L_x/2, L_y/2, 0)$	Q9 FRPM (6x6)	0.0311	0.0303	0.0301	0.0308	0.0305	0.0303
			Q9 FRPM (12x12)	0.0301	0.0289	0.0290	0.0296	0.0294	0.0291
			Q9 FRPM (18x18)	0.0300	0.0288	0.0290	0.0296	0.0294	0.0291
		$\hat{\sigma}_\zeta(L_x/2, L_y/2, 0)$	Q9 FRPM (6x6)	0.1040	0.1051	0.1043	0.1045	0.1041	0.1047
			Q9 FRPM (12x12)	0.1015	0.1018	0.1015	0.1016	0.1015	0.1017
			Q9 FRPM (18x18)	0.1013	0.1015	0.1013	0.1014	0.1013	0.1014
3	10	$\hat{u}_\zeta(L_x/2, L_y/2, 0)$	Q9 FRPM (6x6)	0.4091	0.2490	1.0002	0.3159	0.6658	0.5129
			Q9 FRPM (12x12)	0.4077	0.2472	1.0040	0.3146	0.6651	0.5109
			Q9 FRPM (18x18)	0.4076	0.2470	1.0051	0.3145	0.6654	0.5108
		$\hat{\sigma}_x(L_x/2, L_y/2, 0)$	Q9 FRPM (6x6)	0.0166	0.0160	0.0161	0.0164	0.0163	0.0161
			Q9 FRPM (12x12)	0.0161	0.0155	0.0156	0.0159	0.0158	0.0156
			Q9 FRPM (18x18)	0.0161	0.0154	0.0156	0.0158	0.0158	0.0156
		$\hat{\sigma}_\zeta(L_x/2, L_y/2, 0)$	Q9 FRPM (6x6)	0.0515	0.0517	0.0515	0.0516	0.0515	0.0516
			Q9 FRPM (12x12)	0.0503	0.0503	0.0503	0.0503	0.0503	0.0503
			Q9 FRPM (18x18)	0.0502	0.0503	0.0502	0.0502	0.0502	0.0502

Table 7 shows the Q9 FRPM solutions of displacement and stress components induced at the centers of sandwich FGM plates with various boundary conditions and under a sinusoidally distributed load, in which k_p=1 and 3, S=5 and 10, $L_x = L_y$, and (6x6), (12x12) and (18x18) meshes are used. Again, it can be seen in Table 6 that the convergent solutions are yielded when the Q9 FRPM with (18x18) mesh is used, and the magnitude order of the center deflections of these plates with various boundary conditions is FF>SF>CF>SS>SC>CC.

Figures 6 and 7 show the through-thickness distributions of assorted field variables induced at the position (x, y)=$(L_x/4, L_y/4)$ of the sandwich FGM plates, subjected to a sinusoidally distributed load, for (SS, SC, CC) and (FF, SF, CF) boundary conditions, respectively, in which L_x/h=10, $L_x = L_y$, $h_1 : h_2 : h_3$=0.1h:0.8h:0.1h, and κ_p= 3. For comparison purpose, the scales of each sub-figure are arranged to be identical for each variable. It can be seen in Figs. 6 and 7 that the variation patterns of a typical variable for different boundary conditions are similar to one another, while the differences in their corresponding magnitudes are large, except for the transverse normal stress component, which means the effects of boundary conditions on the displacement and stress components of a sandwich FGM plate are significant. Moreover, these FRPM solutions yield a continuous value for the transverse stress components at the face-sheet/core interfaces of the plate and exactly satisfy the traction conditions on the lateral surfaces, while that is difficult to achieve for other existing PVD-based FEMs when the constitutive equations are used in their computation.

4   Concluding remarks

This work developed a unified formulation of various RMVT-based FRPMs to investigate the static behaviors of multilayered composite plates and sandwich FGM ones with one pair of simply supported opposite edges. In the implementations of these FRPMs, the results show that the Q8 and Q9 FRPM solutions are in excellent agreement with the exact 3D ones for the simply supported laminated composite plates and the FGM ones available in the literature, and that the approach developed in this work has a fast convergence speed. It is also shown that the deviations of the through-thickness distributions of assorted field variables among single-layered homogeneous ($\kappa_p = 0$), sandwich homogeneous ($\kappa_p = \infty$), and sandwich FGM plates ($\kappa_p \neq 0$ and ∞) quite differ significantly from one another, and these observations may provide a reference for the kinetic and kinematic assumptions a priori when the advanced 2D theoretical approaches and numerical models are developed for FGM plates. Moreover, it is concluded that the performance of sandwich FGM plates is superior to that of sandwich homogeneous plates, in that the in-plane stress components are continuous through the face sheet/core interfaces for sand-
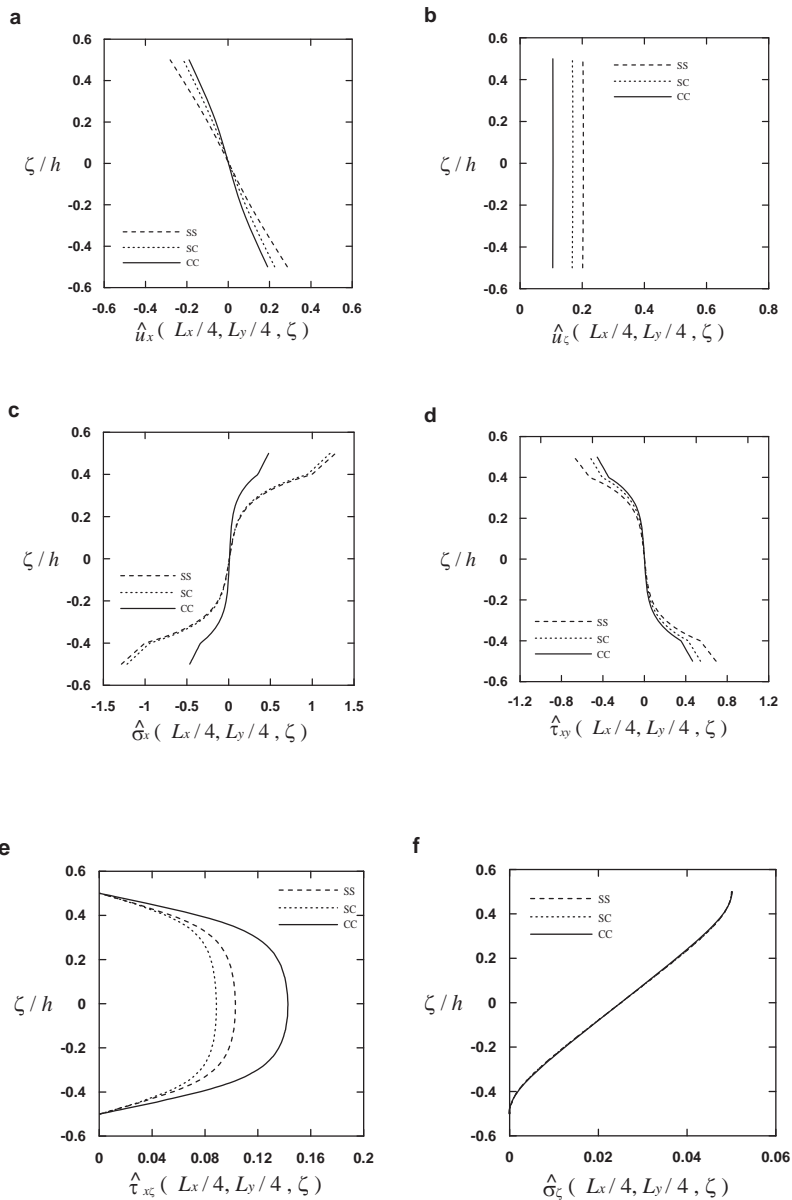
Figure 6: The Q9 FRPM solutions for the through-thickness distributions of various field variables at the $(x = L_x/4, y = L_y/4)$ section of a sandwich FGM plate with SS, SC and CC supports.
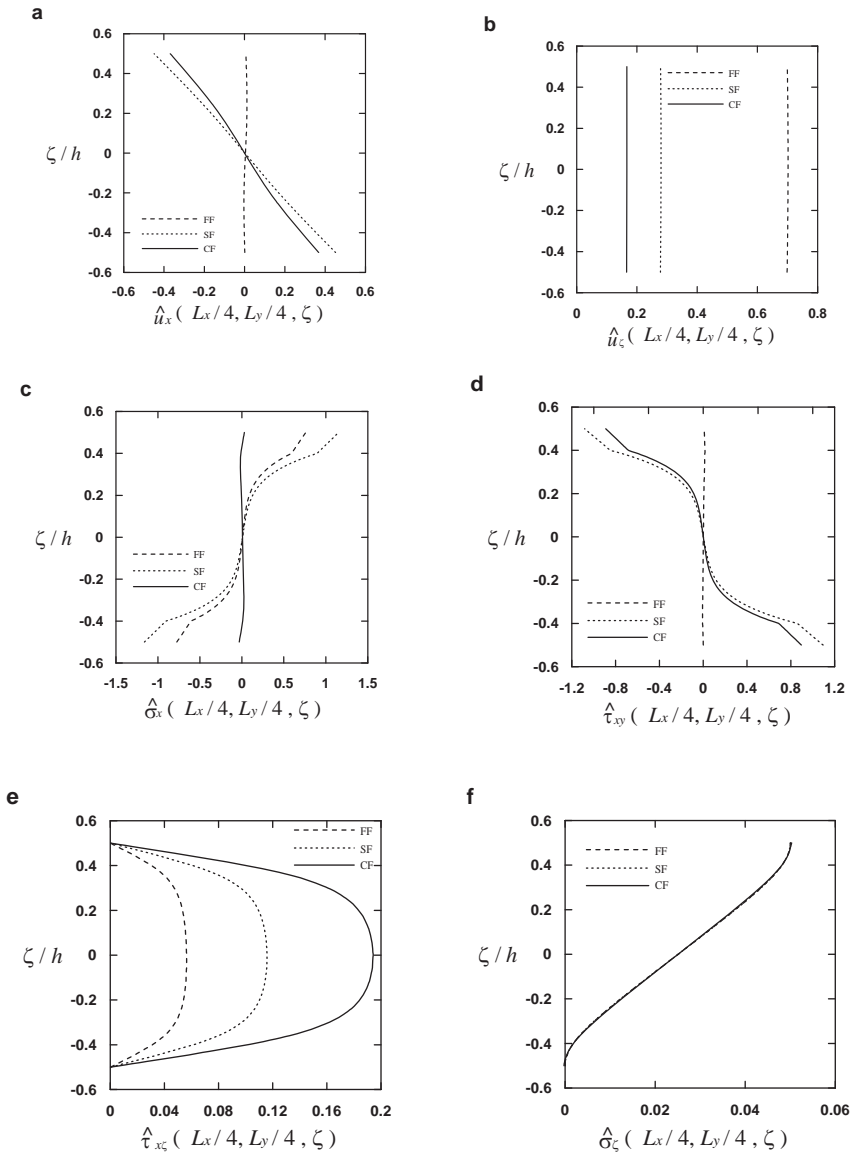
Figure 7: The Q9 FRPM solutions for the through-thickness distributions of various field variables at the $(x = L_x/4, y = L_y/4)$ section of a sandwich FGM plate with FF, SF and CF supports.

wich FGM plates, but abruptly change for the sandwich homogeneous ones, and that the transverse stress components induced at the interfaces between adjacent layers for sandwich FGM plates are significantly reduced as compared with those for sandwich homogeneous plates.

Acknowledgments

References

Ajmi, M.A.; Benjeddou A. (2011): A new discrete-layer finite element for electromechanically coupled analyses of piezoelectric adaptive composite structures. *CMC–Comput. Mater. Continua*, vol. 23, pp. 265–285.

Akhras, G.; Li, W.C. (2007): Three-dimensional static, vibration and stability analysis of piezoelectric composite plates using a finite layer method. *Smart Mater. Struct.*, vol. 16, pp. 561–569.

Akhras, G.; Li, W.C. (2008): Three-dimensional thermal buckling analysis of piezoelectric composite plates using the finite layer method. *Smart Mater. Struct.*, vol. 17, pp. 1–8.

Akhras, G.; Li, W.C. (2010): Three-dimensional stability analysis of piezoelectric antisymmetric angle-ply laminates using finite layer method. *J. Intell. Mater. Sys. Struct.*, vol. 21, pp. 719–727.

Brischetto, S.; Carrera, E. (2010): Advanced mixed theories for bending analysis of functionally graded plates. *Comput. Struct.*, vol. 88, pp. 1474–1483..

Carrera, E. (2000a): An assessment of mixed and classical theories on global and local response of multilayered orthotropic plates. *Compos. Struct.*, vol. 50, pp. 183–198.

Carrera, E. (2000b): A priori vs. a posteriori evaluation of transverse stresses in multilayered orthotropic plates. *Compos. Struct.*, vol. 48, pp. 245–260.

Carrera, E. (2000c): An assessment of mixed and classical theories on global and local response of multilayered orthotropic plates. *Compos. Struct.*, vol. 50, pp. 183–198.

Carrera, E. (2001): Developments, ideas, and evaluations based upon Reissner's Mixed Variational Theorem in the modeling of multilayered plates and shells. *Appl. Mech. Rev.*, vol. 54, pp. 301–329.

Carrera, E. (2003a): Historical review of zig-zag theories for multilayered plates

and shells. *Appl. Mech. Rev.*, vol. 56, pp. 287-308.

Carrera, E. (2003b): Theories and finite elements for multilayered plates and shells: A unified compact formulation with numerical assessment and benchmarks. *Arch. Comput. Methods Eng.*, vol. 10, pp. 215–296.

Carrera, E.; Brischetto, S.; Robaldo, A. (2008): Variable kinematic model for the analysis of functionally graded material plates. *AIAA J.*, vol. 46, pp. 194–203.

Carrera, E.; Brischetto, S.; Cinefra, M.; Soave, M. (2010): Refined and advanced models for multilayered plates and shells embedding functionally graded material layers. *Mech. Adv. Mater. Struct.*, vol. 17, pp. 603–621.

Carrera, E.; Ciuffreda, A. (2005a): Bending of composites and sandwich plates subjected to localized lateral loadings: A comparison of various theories. *Compos. Struct.*, vol. 68, pp. 185–202.

Carrera, E.; Ciuffreda, A. (2005b): A unified formulation to assess theories of multilayered plates for various bending problems. *Compos. Struct.*, vol. 69, pp. 271–293.

Carrera, E.; Demasi, L. (2002a): Classical and advanced multilayered plate elements based upon PVD and RMVT. Part 1: Derivation of finite element matrices. *Int. J. Numer. Methods Eng.*, vol. 55, pp. 191-231.

Carrera, E.; Demasi, L. (2002b): Classical and advanced multilayered plate elements based upon PVD and RMVT. Part 2: Numerical implementations. *Int. J. Numer. Methods Eng.*, vol. 55, pp. 253-291.

Carrera, E.; Petrolo, M. (2010): Guidelines and recommendations to construct theories for metallic and composite plates. *AIAA J.*, vol. 48, pp. 2852–2866.

Chen, J.; Chen, H.; Pan, E. (2006): Free vibration of functionally graded magneto-electro-elastic and multilayered plates. *Acta Mech. Solida Sinica*, vol. 19, pp. 160–166.

Chen, W.Q.; Lüe, C.F. (2005): 3D free vibration analysis of cross-ply laminated plates with one pair of opposite edges simply supported. *Compos. Struct.*, vol. 69, pp. 77–87.

Chen, W.Q.; Lv, C.F.; Bian, Z.G. (2004): Free vibration analysis of generally laminated beams via state-space-based differential quadrature. *Compos. Struct.*, vol. 63, pp. 417–425.

Cheung, Y.K.; Jiang, C.P. (2001): Finite layer method in analysis of piezoelectric composite laminates. *Comput. Methods Appl. Mech. Engrg.*, vol. 191, pp. 879–901.

Cinefra, M.; Belouettar, S.; Soave, M.; Carrera, E. (2010): Variable kinematic models applied to free-vibration analysis of functionally graded material shells.

Eur. J. Mech. A/Solids, vol. 29, pp. 1078–1087.

Demasi, L. (2008): ∞^3 hierarchy plate theories for thick and thin composite plates: the generalized unified formulation. *Compos. Struct.*, vol. 84, pp. 256–270.

Demasi, L. (2009a): ∞^6 mixed plate theories based on the Generalized Unified Formulation, Part I: Governing equations. *Compos. Struct.*, vol. 87, pp. 1–11.

Demasi, L. (2009b): ∞^6 mixed plate theories based on the Generalized Unified Formulation, Part II: Layerwise theories. *Compos. Struct.*, vol. 87, pp. 12–22.

Demasi, L. (2009c): ∞^6 mixed plate theories based on the Generalized Unified Formulation, Part III: Advanced mixed high order shear deformation theories. *Compos. Struct.*, vol. 87, pp. 183–194.

Demasi, L. (2009d): ∞^6 mixed plate theories based on the Generalized Unified Formulation, Part IV: Zig-zag theories. *Compos. Struct.*, vol. 87, pp. 195–205.

Demasi, L. (2009e): ∞^6 mixed plate theories based on the Generalized Unified Formulation, Part V: Results. *Compos. Struct.*, vol. 88, pp. 1–16.

Kashtalyan, M. (2004): Three-dimensional elasticity solution for bending of functionally graded rectangular plates. *Eur. J. Mech. A/Solids*, vol. 23, pp. 853–864.

Kashtalyan, M.; Menshykova, M. (2009a): Three-dimensional elasticity solution for sandwich panels with a functionally graded core. *Compos. Struct.*, vol. 87, pp. 36–43.

Kashtalyan, M.; Menshykova, M. (2009b): Effect of a functionally graded interlayer on three-dimensional elastic deformation of coated plates subjected to transverse loading. *Compos. Struct.*, vol. 89, pp. 167–176.

Liew, K.M.; Ng, T.Y.; Zhang, J.Z. (2002): Differential quadrature–layerwise modeling technique for three-dimensional analysis of cross-ply laminated plates of various edge-supports. *Comput. Methods Appl. Mech. Engrg.*, vol. 191, pp. 3811–3832.

Liu, P.; Zhang, Y.; Zhang, K. (1994): Bending solutions of high-order refined shear deformation theory for rectangular composite plates. *Int. J. Solids Struct.*, vol. 31, pp. 2491–2507.

Lü, C.F.; Chen, W.Q.; Shao, J.W. (2008): Semi-analytical three-dimensional elasticity solutions for generally laminated composite plates. *Eur. J. Mech. A/Solids*, vol. 27, pp. 899–917.

Lü, C.F.; Lim, C.W.; Chen, W.Q. (2009): Semi-analytical analysis for multi-directional functionally graded plates: 3D elasticity solutions. *Int. J. Numer. Methods Eng.*, vol. 79, pp. 25–44.

Noor, A.K.; Burton, W.S. (1990a): Assessment of computational models for mul-

tilayered anisotropic plates. *Compos. Struct.*, vol. 14, pp. 233–265.

Noor, A.K.; Burton, W.S. (1990b): Assessment of computational models for multilayered composite shells. *Appl. Mech. Rev.*, vol. 43, pp. 67–97.

Noor, A.K.; Burton, W.S.; Bert, C.W. (1996): Computational model for sandwich panels and shells. *Appl. Mech. Rev.*, vol. 49, pp. 155–199.

Noor, A.K.; Burton, W.S.; Peters, J.M. (1991): Assessment of computational models for multilayered composite cylinders. *Int. J. Solids Struct.*, vol. 27, pp. 1269–1286.

Pagano, N.J. (1970): Exact solutions for rectangular bidirectional composites and sandwich plates, *J. Compos. Mater.*, vol. 4, pp. 20–34.

Pan, E. (2003): Exact solution for functionally graded anisotropic elastic composite laminates. *J. Compos. Mater.*, vol. 37, pp. 1903–1920.

Pan, E.; Han, F. (2005): Exact solution for functionally graded and layered magneto-electro-elastic plates. *Int. J. Eng. Sci.*, vol. 43, pp. 321–339.

Reissner, E. (1984): On a certain mixed variational theory and a proposed applications. *Int. J. Numer. Methods Eng.*, vol. 20, pp. 1366–1368.

Reissner, E. (1986): On a mixed variational theorem and on a shear deformable plate theory. *Int. J. Numer. Methods Eng.*, vol. 23, pp. 193–198.

Sheng, H.Y.; Ye, J.Q. (2002): A state space finite element for laminated composite plates. *Comput. Methods Appl. Mech. Engrg.*, vol. 191, pp. 4259–4276.

Sheng, H.Y.; Ye, J.Q. (2003): A three-dimensional state space finite element solution for laminated composite cylindrical shells. *Comput. Methods Appl. Mech. Engrg.*, vol. 192, pp. 2441–2459.

Woodward, B.; Kashtalyan, M. (2010): Bending response of sandwich panels with graded core. *Mech. Adv. Mater. Struct.*, vol. 17, pp. 586–594.

Wu, C.P.; Chang, Y.T. (2012): A unified formulation of RMVT-based finite cylindrical layer methods for sandwich circular hollow cylinders with an embedded FGM layer. *Compos. Part B: Eng,* vol. 43, pp. 3318-3333.

Wu, C.P.; Chen, S.J.; Chiu, K.H. (2010): Three-dimensional static behavior of functionally graded magneto-electro-elastic plates using the modified Pagano method, *Mech. Res. Commun.*, vol. 37, pp. 54–60.

Wu, C.P.; Chi, Y.W. (2004): A refined asymptotic theory for the nonlinear analysis of laminated cylindrical shells. *CMC-Comput. Mater. Continua*, vol. 1, pp. 337–352.

Wu, C.P.; Chi, Y.W. (2005): Three-dimensional nonlinear analysis of laminated cylindrical shells under cylindrical bending. *Eur. J. Mech. A/Solids*, vol. 24, pp.

837–856.

Wu, C.P.; Chiu, S.J. (2002): Thermally induced dynamic instability of laminated composite conical shells. *Int. J. Solids Struct.*, vol. 39, pp. 3001–3021.

Wu, C.P.; Chiu, K.H.; Wang, Y.M. (2008): A review of the three-dimensional analytical approaches of multilayered and functionally graded piezoelectric plates and shells. *CMC-Comput. Mater. Continua*, vol. 18, pp. 93–132.

Wu, C.P.; Huang, S.E. (2009): Three-dimensional solutions of functionally graded piezo-thermo-elastic shells and plates using a modified Pagano method. *CMC-Comput. Mater. Continua*, vol. 12, pp. 251–281.

Wu, C.P.; Jiang, T.Y. (2011): The 3D coupled analysis of FGPM circular hollow sandwich cylinders under thermal load. J. *Intell. Mater. Sys. Struct.*, vol. 22, pp. 691–712.

Wu, C.P.; Li, H.Y. (2010a): The RMVT- and PVD-based finite layer methods for the three-dimensional analysis of multilayered composite and FGM plates. *Compos. Struct.*, vol. 92, pp. 2476–2496.

Wu, C.P.; Li, H.Y. (2010b): RMVT- and PVD-based finite layer methods for the quasi-3D free vibration analysis of multilayered composite and FGM plates. *CMC–Comput. Mater. Continua,* vol. 19, pp. 155–198.

Wu, C.P; Li, H.Y. (2010c): An RMVT-based third-order shear deformation theory of multilayered functionally graded material plates. *Compos. Struct.*, vol. 92, pp. 2591–2605.

Wu, C.P.; Liu, K.Y. (2007): A state space approach for the analysis of doubly curved functionally graded elastic and piezoelectric shells. *CMC–Comput. Mater. Continua,* vol. 6, pp. 177–199.

Wu, C.P.; Lu, Y.C. (2009): A modified Pagano method for the 3D dynamic responses of functionally graded magneto-electro-elastic plates. *Compos. Struct.*, vol. 90, pp. 363–372.

Wu, C.P.; Syu, Y.S. (2007): Exact solutions of functionally graded piezoelectric shells under cylindrical bending. *Int. J. Solids Struct.*, vol. 44, pp. 6450–6472.

Wu, C.P.; Syu, Y.S.; Lo, J.Y. (2007): Three-dimensional solutions for multilayered piezoelectric hollow cylinders by an asymptotic approach. *Int. J. Mech. Sci.*, vol. 49, pp. 669–689.

Wu, C.P; Tsai, T.C. (2010): Exact solutions of functionally graded piezoelectric material sandwich cylinders by a modified Pagano method. *Appl. Math. Model.*, vol. 36, pp. 1910–1930.

Wu, C.P.; Tsai, Y.H. (2004): Asymptotic DQ solutions of functionally graded annular spherical shells. *Eur. J. Mech. A/Solids*, vol. 23, pp. 283–299.

Wu, C.P.; Tsai, Y.H. (2007): Static behavior of functionally graded magneto-electro-elastic shells under electric displacement and magnetic flux. *Int. J. Eng. Sci.*, vol. 45, pp. 744–769.

Wu, C.P.; Wu, C.H. (2000): Asymptotic differential quadrature solutions for the free vibration of laminated conical shells. *Comput. Mech.*, vol. 25, pp. 346–357.

Ye, J.Q.; Sheng, H.Y. (2003): Free-edge effect in cross-ply laminated hollow cylinders subjected to axisymmetric transverse loads. *Int. J. Mech. Sci.*, vol. 45, pp. 1309–1326.

Ye, J.Q.; Sheng, H.Y.; Qin, Q.H. (2004): A state space finite element for laminated composites with free edges and subjected to transverse and in-plane loads. *Comput. Struct.*, vol. 82, pp. 1131–1141.

Zenkour, A. (2006): A generalized shear deformation theory for bending analysis of functionally graded plates, *Appl. Math. Model.*, vol. 30, pp. 67–84.

Zhang, J.Z.; Ng, T.Y.; Liew, K.M. (2003): Three-dimensional theory of elasticity for free vibration analysis of composite laminates via layerwise differential quadrature modelling. *Int J. Numer. Methods Eng.*, vol. 57, pp. 1819–1844.

Appendix

The shape functions of the L4, Q8 and Q9 prisms are given as follows:

For a L4 prism, they are

$$\left[\psi_k^{(e)}(\xi,\eta)\right]_1 = \frac{1}{4}(1-\xi)(1-\eta), \quad \left[\psi_k^{(e)}(\xi,\eta)\right]_2^{(e)} = \frac{1}{4}(1+\xi)(1-\eta),$$

$$\left[\psi_k^{(e)}(\xi,\eta)\right]_3^{(e)} = \frac{1}{4}(1+\xi)(1+\eta), \quad \left[\psi_k^{(e)}(\xi,\eta)\right]_4^{(e)} = \frac{1}{4}(1-\xi)(1+\eta),$$

where the subscript k may be u, w, τ or σ; ξ and η are the so-called natural coordinates; and $\xi = \bar{x}/(a/2)$ and $\eta = \bar{\zeta}/(b/2)$.

For a Q8 prism, they are

$$\left[\psi_k^{(e)}(\xi,\eta)\right]_1 = \frac{1}{4}(1-\xi)(1-\eta)(-1-\xi-\eta),$$

$$\left[\psi_k^{(e)}(\xi,\eta)\right]_2 = \frac{1}{4}(1+\xi)(1-\eta)(-1+\xi-\eta),$$

$$\left[\psi_k^{(e)}(\xi,\eta)\right]_3 = \frac{1}{4}(1+\xi)(1+\eta)(-1+\xi+\eta),$$

$$\left[\psi_k^{(e)}(x,z_m)\right]_4 = \frac{1}{4}(1-\xi)(1+\eta)(-1-\xi+\eta),$$

$$\left[\psi_k^{(e)}(\xi,\eta)\right]_5 = \frac{1}{2}\left(1-\xi^2\right)(1-\eta), \quad \left[\psi_k^{(e)}(\xi,\eta)\right]_6 = \frac{1}{2}\left(1+\xi\right)\left(1-\eta^2\right),$$

$$\left[\psi_k^{(e)}(\xi,\eta)\right]_7 = \frac{1}{2}\left(1-\xi^2\right)(1+\eta), \quad \left[\psi_k^{(e)}(\xi,\eta)\right]_8 = \frac{1}{2}\left(1-\xi\right)\left(1-\eta^2\right).$$

For a Q9 prism, they are

$$\left[\psi_k^{(e)}(\xi,\eta)\right]_1 = \frac{1}{4}(1-\xi)(1-\eta)\,\xi\,\eta, \quad \left[\psi_k^{(e)}(x,\eta)\right]_2 = -\frac{1}{4}(1+\xi)(1-\eta)\,\xi\,\eta,$$

$$\left[\psi_k^{(e)}(\xi,\eta)\right]_3 = \frac{1}{4}(1+\xi)(1+\eta)\,\xi\,\eta, \quad \left[\psi_k^{(e)}(x,z_m)\right]_4^{(m)} = -\frac{1}{4}(1-\xi)(1+\eta)\,\xi\eta,$$

$$\left[\psi_k^{(e)}(\xi,\eta)\right]_5 = -\frac{1}{2}\left(1-\xi^2\right)(1-\eta)\,\eta, \quad \left[\psi_k^{(e)}(\xi,\eta)\right]_6 = \frac{1}{2}\left(1+\xi\right)\left(1-\eta^2\right)\xi,$$

$$\left[\psi_k^{(e)}(\xi,\eta)\right]_7 = \frac{1}{2}\left(1-\xi^2\right)(1+\eta)\,\eta, \quad \left[\psi_k^{(e)}(\xi,\eta)\right]_8 = -\frac{1}{2}\left(1-\xi\right)\left(1-\eta^2\right)\xi,$$

$$\left[\psi_k^{(e)}(\xi,\eta)\right]_9 = \left(1-\xi^2\right)\left(1-\eta^2\right).$$